

# Simulating Electron Transport and Synchrotron Emission in Radio Galaxies: Shock Acceleration and Synchrotron Aging in Three-Dimensional Flows

I. L. Tregillis<sup>1</sup>, T. W. Jones<sup>1</sup>, Dongsu Ryu<sup>2</sup>

## ABSTRACT

We present the first three-dimensional MHD radio galaxy simulations that explicitly model transport of relativistic electrons, including diffusive acceleration at shocks as well as radiative and adiabatic cooling in smooth flows. We discuss here three simulations of light Mach 8 jets, designed to explore the effects of shock acceleration and radiative aging on the nonthermal particle populations that give rise to synchrotron and inverse-Compton radiations. Because our goal is to explore the connection between the large-scale flow dynamics and the small-scale physics underlying the observed emissions from real radio galaxies, we combine the magnetic field and relativistic electron momentum distribution information to compute an approximate but self-consistent synchrotron emissivity and produce detailed synthetic radio telescope observations.

We have gained several key insights from this approach: 1. The jet head in these multidimensional simulations is an extremely complex environment. The classical jet termination shock is often absent, but motions of the jet terminus spin a “shock-web complex” within the backflowing jet material of the head. 2. Correct interpretation of the spectral distribution of energetic electrons in these simulations relies partly upon understanding the shock-web complex, for it can give rise to distributions that confound interpretation in terms of the standard model for radiative aging of radio galaxies. 3. The magnetic field outside of the jet itself becomes very intermittent and filamentary in these simulations, yet adiabatic expansion causes most of the cocoon volume to be occupied by field strengths considerably diminished below the nominal jet value. Radiative aging is very slow in these volumes, so population aging rates vary considerably from point to point. 4. Overall, the intricate dynamical behaviors in these

---

<sup>1</sup>School of Physics and Astronomy, University of Minnesota, Minneapolis, MN 55455: tregilli@msi.umn.edu; twj@msi.umn.edu

<sup>2</sup>Department of Astronomy & Space Science, Chungnam National University, Daejeon, 305-764 Korea: ryu@canopus.chungnam.ac.kr

models make it difficult to capture the histories of the nonthermal particles in broad generalizations. Understanding even the simplest of these models requires attention to details of the flow.

*Subject headings:* galaxies: jets — MHD — radiation mechanisms: nonthermal  
— radio continuum: galaxies

## 1. INTRODUCTION

The jet-based dynamical model for the structure of radio galaxies has found great support over nearly three decades of ever-increasing observational and theoretical scrutiny. Unfortunately, however, some of the basic physics attendant upon this model remains elusive. The key idea, that lobes of luminous material identify the interaction between an ambient environment and a high-velocity plasma jet launched within an active galactic nucleus (*e.g.*, Blandford & Rees 1974; Scheuer 1974; Begelman, Blandford, & Rees 1984; Bridle 1992), accounts for an impressive array of observed properties. It is similarly well-known that the characteristic radio emission signals the presence of magnetic fields and relativistic electrons. However, the source of these two ingredients, whether they are transported along the jet, or introduced in the jet-IGM encounter, or both, is not well understood. The physics of powerful radio galaxies requires not only the presence of relativistic particles, but also their reacceleration. At least in some sources, hotspot brightnesses cannot be accounted for simply through adiabatic compression (*e.g.*, Cygnus A, Pictor A). Similarly, the energetics of X-ray emission observed from hotspots and knots in some radio galaxies also requires relativistic particle acceleration. Yet the details of the reacceleration process inside radio galaxies are largely unknown. Indeed, there is a significant gap in our understanding of the detailed manner in which the macrophysics of large-scale flows feeds the microphysics of synchrotron and X-ray emission.

Great advances in computational modeling have made it possible to perform sophisticated multidimensional hydrodynamical (HD) and magnetohydrodynamical (MHD) numerical simulations (*e.g.*, Clarke, Norman, & Burns 1989; Lind, Payne, Meier, & Blandford 1989; Kössl, Müller, & Hillebrant 1990; Clarke 1996; Nishikawa, Koide, Sakai, Christidou, Sol, & Mutel 1998). Jones, Ryu, & Engel (1999, hereafter JRE99) presented the first such simulations to include explicit time-dependent transport of the relativistic electrons responsible for the radio emission observed from such sources. That work introduced a novel, computationally economical scheme for treating relativistic particle transport, and applied it to ideal, axisymmetric MHD flows. The scheme includes the effects of diffusive shock acceleration, radiative cooling, and adiabatic effects on the electrons in smooth flows. The addition of

this new energetic particle transport feature to computational models of radio galaxy evolution provided a key ingredient needed to bridge the gap between simulation of large-scale plasma flows and simulation of the emissions that result. JRE99 demonstrated that information about the nonthermal particle distribution could be combined with the magnetic field structure in the MHD flows to compute an approximate synchrotron emissivity in each computational zone. By doing so those authors were able to investigate the distribution of synchrotron emissivities and spectral indices throughout the simulated flows. The effort of JRE99 was concentrated on addressing the individual dynamical influences on the shock acceleration of radio galaxy electrons as a way to characterize and recognize signs of shock acceleration in these environments.

This paper presents the extension of that work into three dimensions. We continue to place our emphasis upon recognizing and characterizing the signs of shock acceleration and radiative aging in the complex flows that are expected to reside within radio galaxies. This work is, therefore, a first attempt at combining an understanding of the flow dynamics with the subsequent particle transport effects in three dimensions. The notorious complexity of driven, multidimensional plasma flows (Sato & The Complexity Simulation Group 1996) forces us here to restrict our attention to a small region of the available parameter space; we defer to later papers the treatment of more detailed and specific questions. Our long-term goal is to identify specific physical processes that lead to observed structures in radio galaxies, and vice-versa.

Using the previous results in two dimensions as a guide for exploration, we also utilize the nonthermal particle transport scheme in a new way by creating the first synthetic observations to include explicitly calculated nonthermal electron distributions. Preliminary results of this synthetic observation work were reported in Tregillis, Jones, & Ryu (2001a, in press) and Tregillis, Jones, Ryu, & Park (2001b, in press). The earliest attempts to obtain emission characteristics from purely hydrodynamical calculations estimated the local magnetic field strength and the distribution of nonthermal particles by assuming a simple relation with the local gas density (Smith, Norman, Winkler, & Smarr 1985). Matthews & Scheuer (1990a,b) showed that the details of radio hotspot structures are not revealed by investigation of the interior pressure distribution. However the hotspot structures seen in images created by projecting the maximum density or pressure along each line of sight through a simulation of a precessing HD jet (Cox, Gull, & Scheuer 1991) can show impressive similarity to the multiple hotspots observed in numerous real sources (Lonsdale & Barthel 1986; Looney & Hardcastle 2000). Hughes, Duncan, & Mioduszewski (1996) concluded that purely HD simulations can never truly model the jet synchrotron emission, at least for relativistic flows. The inclusion of a vector magnetic field improves the situation by making possible the calculation of polarization properties (*e.g.*, Laing 1981; Clarke et al. 1989) within an

assumed emissivity model. But even fully three-dimensional MHD simulations require the exercise of critical assumptions before an emissivity can be constructed from fluid variables (*e.g.*, Clarke 1993). Further, even at this level of sophistication there is no means by which the emission spectrum can be obtained, although Matthews & Scheuer (1990a) were able to address the issue of deviation from a strict power law distribution of particles by assuming no distributed particle acceleration and introducing a synchrotron loss parameter associated with a fluid element. The necessary information about the nonthermal particle distribution requires specific treatment of the essential electron microphysics that comes naturally out of the particle transport scheme we utilize here.

An intermediate approach to obtaining emissivities is offered by Kaiser and collaborators (Kaiser 2000), for example. That work developed an analytical model for surface brightness distributions in the cocoons of FRII-type radio galaxies, based on self-similar, axisymmetric models of evolution. The method extends classical spectral aging methods by taking into account the detailed loss histories of the emitting particles, as ours does explicitly, also. Magnetic field and cosmic-ray distributions throughout the source must be assumed within self-similar models such as these. In our models these distributions are allowed to evolve naturally from the initial conditions imposed at the beginning of the calculation.

The remainder of this paper will proceed as follows. §2 outlines our methods, and provides an overview of the electron-transport scheme originally presented in JRE99. The details of our models and the physical parameters characterizing our simulated jets are given in §3, and the results are discussed in §4, concentrating first upon the jet dynamics and then turning to consideration of the effects upon energetic particle transport. The key findings are summarized in §5.

## 2. METHODS

### 2.1. Dynamics

We evolve the equations of ideal nonrelativistic magnetohydrodynamics (MHD) in Cartesian coordinates  $(x, y, z)$ . All three components of velocity and magnetic field are included, so the model is truly three-dimensional. The code is an MHD extension of Harten’s (Harten 1983) conservative, second-order finite difference “total variation diminishing” scheme, as detailed in Ryu & Jones (1995) and Ryu et al. (1995). The code preserves  $\nabla \cdot B = 0$  at each time step using an approach similar to the upwinded constrained transport (CT) scheme (Evans & Hawley 1988) as described in detail by Ryu, Miniati, Jones, & Frank (1998). We use a passive “mass fraction” or “color tracer”,  $C_j$ , to distinguish material entering the grid

through the jet orifice ( $C_j = 1$ ) from ambient plasma ( $C_j = 0$ ).

## 2.2. Electron Transport

We present the general flavor of our electron transport scheme here, and refer the reader to the extensive discussion of the method in JRE99. Energetic particle transport is treated using the conventional convection-diffusion equation for the momentum distribution function

$$\frac{\partial f}{\partial t} = \frac{1}{3} p \frac{\partial f}{\partial p} (\nabla \cdot \mathbf{u}) - \mathbf{u} \cdot \nabla f + \nabla \cdot (\kappa \nabla f) + \frac{1}{p^2} \frac{\partial}{\partial p} \left( p^2 D \frac{\partial f}{\partial p} \right) + Q \quad (1)$$

(*e.g.*, Skilling 1975). Here  $\mathbf{u}$  is the bulk velocity of the thermal plasma,  $Q$  is a source term representing the effects of injection and radiative losses,  $D$  and  $\kappa$  are the momentum and spatial diffusion and coefficients, and  $f(\mathbf{x}, p, t)$  is the isotropic part of the nonthermal electron distribution. This follows spatial and momentum diffusion as well as spatial and momentum advection of the particles. The momentum advection corresponds to energy losses and gains from processes like adiabatic expansion as well as synchrotron aging.

Equation 1 is dominated by the convective terms in smooth flows, because the electron diffusion lengths are much smaller than the dynamical lengths. However the diffusive terms are included because when integrated across a velocity discontinuity (equation 1 is not valid inside shocks) the first three terms on the right-hand side account for first-order Fermi acceleration at shocks (so-called “diffusive shock acceleration”). The first term accounts for adiabatic effects in the flow. The fourth term accounts for second-order Fermi acceleration, although we have not included it in the simulations presented here.

The essence of our scheme takes advantage of the fact that there is a strong mismatch between the scales relevant to dynamical and diffusive transport processes for electrons of relevance to radio and X-ray emissions within radio galaxies. The lengths and times appropriate to the dynamics are orders of magnitude larger than those for electron diffusion at energies relevant to radio synchrotron radiation. (Thus the convective terms in equation 1 dominate the relativistic electron transport in smooth flows.) As a typical example, the gyroradius of a 10 GeV electron in a  $10\mu\text{G}$  magnetic field is  $r_g \approx 3 \times 10^{11}$  cm. Scattering lengths within several orders of magnitude of this scale yield diffusion lengths smaller than the solar system and acceleration timescales  $\lesssim 1$  yr at a typical fast shock. Dynamical scales, however, are generally measured in kpc and kyr, and often much larger scales.

While this discrepancy makes solving equation 1 impractical with conventional computational methods, it can be used to develop a simplified and efficient electron transport equation, valid where  $f(p)$  is sufficiently broad that it is adequately represented as a piece-

wise power law over finite momentum bins. The key point here is that the comparatively miniscule length- and time-scales for electrons make this a natural assumption, since rapid diffusive shock acceleration for  $\lesssim 10$  GeV electrons ensures that they will emerge from shocks with power-law momentum distributions effectively instantaneously compared to the overall dynamics. Subsequent cooling taking place downstream can be treated in a straightforward way. We therefore divide the momentum domain into a small number  $N$  of logarithmically spaced bins, and estimate particle fluxes across momentum bin boundaries by representing  $f(p) \propto p^{-q(p)}$  within bins, where  $q(p)$  varies in a regular way. Numerically, for each bin we use the total number of electrons within that bin and the associated mean logarithmic slope; the computational cost for a modest number of bins (we typically use 8) is comparable to that required for tracking the dynamics, and therefore not prohibitive. Standard finite-difference schemes for solving equation (1) would require more than an order-of-magnitude greater computational effort. The scheme employed in the present simulations has been enhanced over the original version described in JRE99. Most importantly, we have been able to remove the constraint on the original scheme that limited the change in slope from one momentum bin to the next. Thus, spectral cutoffs due to aging are handled better in the current scheme. Otherwise, the methods are the same as employed there. Detailed tests were presented in that paper.

In the test-particle limit for diffusive shock acceleration, electrons emerge from shocks with a power law spectral index  $q = \frac{3r}{r-1}$  where  $r$  is the shock compression ratio. We allow injection of electrons from the thermal plasma at shocks using a model wherein a fixed fraction  $\epsilon$  of the total electron flux through a shock is injected and accelerated to the appropriate power-law distribution beginning at momenta just above the postshock electron thermal values. Here  $\epsilon$  is set to 0 for models 1 and 3, and  $10^{-4}$  for model 2. Electron injection at shocks is not well understood at present. However, nonlinear models of strong shocks usually lead to proton injection values  $\sim 10^{-3}$  (*e.g.*, Gieseler & Jones 2000). Combined with the relative electron injection ratio of a few percent estimated by Bykov and Uvarov (Bykov & Uvarov 1999), a value of  $10^{-4}$  in our simulation is very reasonable. We note, of course, since the electron population in the simulations is passive, that results could be rescaled for an alternate  $\epsilon$ . In any case, if the jet flow consists mostly of “thermalized” plasma, our current understanding of collisionless shocks places  $\epsilon > 0$ . We include simulations both with  $\epsilon = 0$  and  $\epsilon > 0$ , since our purpose here is to explore the importance of including this feature in the simulations.

Our transport approach is complementary to that described by Micono et al. (1999). There, the convection-diffusion equation was followed in detail outside of shocks using conventional numerical methods, but the calculation was constrained to follow a small number of selected Lagrangian volume elements in the flow because of high numerical costs. While that

method is not reliant upon the assumption of a piecewise power law momentum distribution, it does not make possible synthetic observations of the simulated flows, whereas ours does. Another complementary approach is offered by Downes, Duffy, & Komissarov (2001). Those authors also treat the particle acceleration as an injection process by specifying the fraction of the thermal particle flux converted to nonthermal particles at shocks. There the Liouville equation is numerically integrated for particles accelerated in relativistic shocks, rather than solving the diffusion-convection equation directly. That method is computationally efficient; however it does not allow for self-consistent reacceleration of previously-accelerated particles (T. Downes 2000, private communication). The use of a purely hydrodynamic code forces an assumption about the partitioning of post-shock thermal energy between energetic particles and the magnetic field in order to model synchrotron emission. Our work is restricted to the consideration of nonrelativistic shocks.

### 3. SIMULATED JET PROPERTIES

Our simulated MHD jets described here are all dynamically identical. Each enters the grid with a simple “top hat” velocity profile and a core speed that is Mach 80 with respect to the uniform ambient medium ( $M_j = u_j/c_a = 80$ ). The high-velocity core is insulated from the ambient medium by a narrow, three-zone-thick transition layer. The jets are initially in approximate pressure balance with the ambient medium and have a density contrast  $\eta = \rho_j/\rho_a = 10^{-2}$ . Thus the jet-based Mach number is 8. The jet enters at  $x = 0$ , with an initial core radius,  $r_j$ , of 15 zones, while the entire grid is  $576 \times 192 \times 192$  uniform zones ( $38\frac{2}{5}r_j \times 12\frac{4}{5}r_j \times 12\frac{4}{5}r_j$ ). Defining length and time in units of initial jet radius ( $r_j = 1$ ) and ambient sound speed ( $c_a = (\gamma P_a/\rho_a)^{1/2} = 1$ , with  $\gamma = 5/3$ ), the simulations are followed for 5.4 time units, at which time the bow shock reaches the boundary at  $x = 38\frac{2}{5}$ . Because our objectives depend on maintaining a fine resolution of the dynamical structures in the simulated jets and their interiors, the large effort inherent in these simulations constrains us to look at relatively young flows for the time being. There is an initial axial background magnetic field ( $B_y = B_z = 0$ ;  $B_x = B_{x0}$ ), with a magnetic pressure 1% of the gas pressure ( $\beta = 10^2$ ). This results in an initial jet Alfvénic Mach number of  $M_{Aj} = 70$  compared to the hydrodynamic Mach 8 figure above. In addition to the axial component  $B_{x0}$ , the inflowing jet also carries a toroidal magnetic field component representing a uniform axial current within the jet, with a return current on the jet surface; i.e.,  $B_\phi = 2 \times B_{x0}(r/r_j)$  for  $r \leq r_j$ .

Open boundary conditions are used everywhere except at the orifice where jet material enters the grid. Another commonly-used boundary condition places a reflecting boundary outside the jet orifice at  $x = 0$  (e.g., Norman 1996). We adopt the open boundary at  $x = 0$

with an eye towards the interpretation that the jet orifice is not a meaningful model of the true jet origin, and instead represents where the collimated jet enters our grid after having been launched further upstream ( $x < 0$ ). Cox et al. (1991) point out that the reflecting boundary at  $x = 0$  is not a true representation of a source with point symmetry about the jet origin, but is a very reasonable approximation for small precession angles.

As described below, we find very high backflow velocities in the cocoon. While consistent with expectations based on general physical arguments, the backflow structure might have been different had we instead used a reflecting boundary at  $x = 0$ . In that case weak shocks might be more likely to form in the supersonic backflow. The open boundary near the jet orifice also contributes to the cocoon pressure and temperature gradients described in §4.1. Because the oldest backflow material leaves the grid prior to the end of the simulation, the remaining cocoon gas has less time during which to come to equilibrium with the ambient medium. Nevertheless, our main conclusions are not significantly affected by the choice of boundary conditions.

Norman (1996) found in 3D jet simulations that even in the absence of an explicitly applied perturbation to the jet velocity, symmetry will eventually be broken by the action of Kelvin-Helmholtz instabilities on the jet, seeded by perturbations from pockets of supersonic turbulence in the cocoon. We found that a dynamically identical run to those presented here differing only in a lack of precession remained essentially two-dimensional for sufficiently long times as to make this approach very expensive for study of three-dimensional behaviors. Thus, to break cylindrical symmetry, we add a modest precession to the in-flowing jet velocity.

In fact, evidence for precession is seen in a number of extragalactic sources (*e.g.*, Condon & Mitchell 1984; Kellermann & Owen 1988; Mantovani et al. 1999; Sudou & Taniguchi 2000). Models for explaining the physical basis of precession in both galactic and extragalactic sources have been discussed in the literature (*e.g.*, van den Heuvel et al. 1980; Spruit 2000). The jets presented here were precessed on a cone of opening angle  $5^\circ$ , as in the first simulation presented in Cox et al. (1991). The precession frequency was chosen so that the jet inflow velocity has just completed 5 revolutions by the end of the run. As discussed in section 4.1 below, we concluded that precession at this frequency was slow enough to avoid undesirable effects from “overspinning” the jet such as excitation of undesirable stabilizing normal modes (Hardee & Rosen 1999), while still breaking symmetry.

We present here three examples of electron transport within the dynamics of the above jet flows. Their properties are listed in Table 1. The essential character of these models was chosen to be analogous to the axisymmetric models explored in the earlier axisymmetric work of JRE99. Electrons are modeled explicitly in the momentum range  $p_0 < p < p_N$  with  $p_0 =$



$10 m_e c$  and  $p_N \approx 1.63 \times 10^5 m_e c$  for all models. Below  $p_0$  the spectrum is assumed to continue as a simple power law, providing the necessary momentum-space boundary condition. The boundary condition at  $p_N$  was set by assuming  $\frac{dq(p_N)}{d \ln p}$  continuous. Eight momentum bins ( $N = 8$ ) were used for each of these models, yielding  $\ln(p_{i+1}/p_i) = 1.5$  for all models. Since the nonthermal cosmic-ray electrons are passive within our simulations, all results could be rescaled for different choices of  $p_0$  ( $p_N/p_0$  is fixed). All three models include the effects of adiabatic cooling and diffusive shock acceleration upon the cosmic-ray electron populations. Second-order Fermi acceleration and nonradiative energy losses such as Coulomb losses are neglected.

In all three models, the nonthermal particle population entering the jet from the orifice comes with a momentum index  $q = 4.4$ , which represents a synchrotron spectral index of  $\alpha = (q - 3)/2 = 0.7$ , where  $S_\nu \propto \nu^{-\alpha}$ .

Models 1 and 2 are “adiabatic” models, in the sense that the electrons experience negligible synchrotron aging in these models, resulting in little spectral curvature. Some curvature can result from spatial mixing, however. Models 1 and 3 are also similar to each other, since the electron populations in these models originate entirely within the in-flowing jet. The ratio of nonthermal to thermal particle number densities in the jet,  $\delta$ , was set to  $10^{-4}$  in these models. Model 2 is distinguished from the other models in that the electron population is mostly injected locally from thermal plasma at shocks within the simulated flow ( $\delta = 10^{-8}$ ,  $\epsilon > 0$ ); this local injection of fresh particles was turned off ( $\epsilon = 0$ ) for models 1 and 3. Model 3 differs from the others via significant radiative aging from synchrotron and inverse-Compton processes.

In order to include the effects of synchrotron aging, the characteristic cooling time  $\tau_{s0}$  must be defined in the computational time units,  $r_j/c_a$ . Following the treatment in JRE99, we express the cooling time in terms of the particle momentum and local magnetic field as

$$\tau_s = \tau_{s0} \frac{\hat{p}}{p} = 25 \frac{1}{p_4} \frac{u_{j8}}{M_j} \frac{1}{r_{jk}} \frac{1}{(B_{10}^2 + B_{cmb}^2)} \quad (2)$$

where  $\hat{p}$  is a convenient fiducial momentum,  $p_4$  is the electron momentum in units of  $10^4 m_e c$ ,  $u_{j8}$  is the jet speed in units of  $10^8 \text{ cm s}^{-1}$ ,  $M_j$  is the jet Mach number in the ambient medium,  $r_{jk}$  is the inflowing jet radius in kpc,  $B_{10}$  is the field strength in units of  $10 \mu\text{G}$  (nT), and  $B_{cmb}$  ( $= 3.2 \mu\text{G} \times (1+z)^4$ ) is the equivalent magnetic field of the cosmic microwave background at redshift  $z$ . All of the models depicted here were chosen to have  $M_j = 80$  as noted above, as well as  $r_{jk} = 2$  and  $u_{j8} = 15$ , which corresponds to  $0.05c$ . This makes the length of our computational box about 77 kpc, and the time unit  $r_j/c_a \sim 10^7$  yr.

Picking a fiducial momentum  $\hat{p} = 10^4$  ( $p_4 = 1$ ), the cooling rate is then parameterized by the field  $B_{10}$ . For models 1 and 2, we have set  $\tau_{s0} = 1.6 \times 10^3$  (compared to 5.4 as

the length of the simulation) by setting  $B_{x0} = 0.39\mu\text{G}$  and ignoring the contribution from inverse Compton scattering off of the cosmic microwave background, the intent being to ensure negligible aging for electrons of interest within the length of the simulations.

On the other hand, for model 3 we set  $B_{x0} = 5.7\mu\text{G}$ , which corresponds to  $\tau_{s0} = 5.4$ . The contribution from the cosmic microwave background is taken into account by setting  $B_{cmb} = 3.2\mu\text{G}$  corresponding to the current epoch. Thus, for this model, aging effects are significant for the electron energy range of interest.

Note that the characteristic cooling time  $\tau_{s0}$  depends very strongly on the redshift,  $z$ , once Compton scattering from the cosmic microwave background becomes important. Thus inverse-Compton losses can lead to significant cooling in high-redshift sources, even if the magnetic fields are relatively weak. In fact for high  $z$ , it is difficult to scale simulations like these such that the nominal cooling time is on the order of the simulation duration (as it is in model 3) without making the jet speed  $u_{j8}$  relativistic, as required by our code.

## 4. DISCUSSION

### 4.1. Flow Dynamics

Here we sketch out the key dynamical behaviors of the simulations, taking advantage of the fact that all three models are dynamically identical. As expected for strongly-driven nonequilibrium systems (Sato & The Complexity Simulation Group 1996) and as has been seen in previous jet simulation work (Norman et al. 1982; Williams & Gull 1985; Lind et al. 1989; Hardee & Norman 1990; Cox et al. 1991; Clarke 1996), the dynamics is often characterized by very complex, nonsteady flows. JRE99 found that nearly all structures in their axisymmetric models were highly variable. We find this to be equally true in the three-dimensional calculations as well, but while the end result (extreme variability of the flow) is rather similar in 2D and 3D the underlying physical processes are quite different.

One of the most prominent characteristics of both two- and three- dimensional jets is a seemingly chaotic, nonsteady jet termination shock. In both cases the jet terminus is so strongly perturbed at some times that it is nearly impossible to identify a strong terminal shock at all. In two dimensions, this arises from the intermittent interaction between oblique shocks within the jet, the Mach stem, and vortices shed from the jet. This interaction gives rise to dramatic fluctuations in the size, strength, and location of the terminal shock, causing it to disappear almost entirely at some times, as well as inducing significant variations in the advance speed of the jet terminus. The spectral distributions of the nonthermal particle populations processed by these shocks are correspondingly intricate. In two dimensions the

role of the oblique shocks may be overemphasized by the axisymmetry, which acts to focus them upon the jet axis.

In three dimensions the nonsteady nature of the terminal shock is even more profound. At the earliest times, the jet structure is nearly axisymmetric, with a clearly defined Mach disk terminating the jet flow and a nice symmetrical backflow (figure 1a, inset) as has been seen in even the earliest two-dimensional calculations (*e.g.*, Norman et al. 1982). The Mach disk is disrupted rather abruptly once the first set of oblique shocks converge upon the jet axis (Clarke 1996) which occurs at approximately  $t = 1$  in our time units, corresponding both to one sound-crossing time and coincidentally to one complete revolution of the precessed inflow velocity. Unlike the two-dimensional case, however, the Mach disk is never recovered after its initial disruption. This is very easily seen in the relevant animation found on our web site <sup>3</sup>. Present on this site are volume-rendered animations of velocity divergence, velocity magnitude, and magnetic pressure. Many of the dynamical behaviors detailed in this section can be viewed directly in these animations.

From that point on, the terminal structure of the jet is better described as a “shock-web complex” rather than as a simple strong terminal shock (figure 1a). This complex encompasses a network of shocks of varying strengths and sizes spread throughout the source, including the head region and backflow. Rapid spatial and temporal changes in the structure of the complex attest to the fleeting nature of many shocks in the system. At the times when the end of the jet truly is associated with a simple terminal shock, that shock is typically too small to capture most of the material passing from the jet into the cocoon. Furthermore, the strongest shock in the system is often not the terminal shock. Therefore, in these simulated flows it does not make sense to describe particle acceleration predominantly in terms of the canonical jet terminal shock. Our code accurately captures strong shocks within 2-3 computational zones (Ryu & Jones 1995), so we are confident that the variety of shock strengths is not an effect of numerical viscosity. These methods do not employ a numerical viscosity, in fact, so shock jumps are quite accurate.

While still present in three dimensions, the oblique shocks within the jet exercise far less control over the overall jet dynamics. In addition, we find several other kinds of shocks arising at different times and locations within the flow. Precession (or more generally any terminal jet “wobble” such as that which arises naturally from fluid instabilities) plays an important role here. At some times the terminal jet velocity is oriented such that the beam “splashes” or “splatters” against the contact discontinuity that forms the cocoon boundary. In these instances the jet impinges on the cocoon boundary at an angle less than the

---

<sup>3</sup><http://www.msi.umn.edu/Projects/twj/radjet/radjet.html>

maximum bending angle (the angle beyond which bending causes disruption of the jet (Icke 1991, eq. 5.58)) and is redirected supersonically back into the cocoon, occasionally even impinging upon the far wall, as has been seen previously by Williams & Gull (1985) and Cox et al. (1991). These “jet redirection events” are visible in images of velocity divergence as intermediate-strength shocks on the cocoon boundary and as magnetic field enhancements in images of magnetic pressure. At other times, the combined actions of wobble and fluid instabilities cause the jet (as identified by a relatively well-collimated high-velocity core; see figure 1b) to develop severe bends, sometimes in excess of the maximum bending angle. Examination of purely hydrodynamical considerations places this value at roughly  $70^\circ$ . In these cases the bending is a precursor to “breaking” and realignment of the jet flow. When this happens the portion of the beam downstream of the “elbow” is disconnected from the main flow and deposited in the backflow; lacking an energy source, this flow quickly dissipates. (This, in fact, is one mechanism for introducing relatively large amounts of new jet material quickly into the backflow. It also provides an energy supply for some of the radio hotspots that occur in the synthetic observations, as discussed in section 4.3.1.) Following disconnection, this “elbow” itself produces a strong, transient terminal shock: the new end of the jet is now straight and pointed roughly towards the end of the cocoon rather than the edges. Note that the terminal shock forms in this case after the bending has become significant, and thus the material downstream of the elbow can enter the backflow without being processed via the shock. The temporary reappearance of the terminal shock is accompanied by the rapid extension of the lobe as seen in the “dentist’s drill” model of Scheuer (1982), and the creation of a narrow “finger” that pokes out of the contact discontinuity where the jet surges forward, resulting in a corresponding deformation and temporary strengthening of the bow shock. In fact, the bow shock is occasionally among the strongest shocks in the system during these events.

In contrast to the situation in three dimensions, instances of disruption and reformation of the terminal shock in two-dimensional simulations were coincident with distinct episodes of strong vortex shedding. In these episodes large “rolls” of material are thrown into the backflow, where they interact with the Kelvin-Helmholtz unstable boundary layer of the jet, further perturbing the jet flow. Axisymmetry in this case forces the shed vortices to be strictly annular, thereby artificially enhancing their effect on the jet. In three dimensions, the vortex structures are stretched and tangled more completely, leading to turbulence and disorder on smaller scales, in turn giving rise to vortex tubes. The turbulent cascade of energy and disorder to smaller scales in the three-dimensional calculation causes instances of extended structures in the backflow acting coherently on the jet to be more unlikely than in two dimensions. On the other hand, the enforced axisymmetry of the two-dimensional calculation allows the jet to experience only pinching modes, such as those driven by shedding of the

annular vortices, while the three-dimensional calculation makes the jet susceptible to a much larger range of possible dynamical modes, including pinching, bending, and twisting modes (*e.g.*, Hardee, Clarke, & Rosen 1997). While not as effective as the asymmetric backflow in slab-symmetric calculations (*e.g.*, Hardee & Norman 1990), the turbulent three-dimensional backflow does contribute strongly to the “flapping” of the jet by providing perturbations that seed these unstable modes. Instances where large amounts of jet material are quickly introduced into the backflow as in the vortex shedding events in two dimensions are not seen as frequently in three-dimensional calculations, although the previously mentioned “breaking” of the jet terminus can have a similar effect.

As the beam grows in length, precession at the inflow boundary is transmitted down the jet as increasingly larger changes in the velocity direction over the precession period, further contributing to the “flapping” of the jet, particularly at the latest times. As mentioned above, earlier simulations (Norman 1996) have shown that three-dimensional hydrodynamical jets ( $M_j = 100, \eta = 10^{-2}$ ) will eventually begin to flap in the absence of precession. There the timescale for side-to-side deflection of the jet occurred on the internal dynamical timescale,  $r_{cocoon}/c_{cocoon}$ , which in that case was 4 – 5 times shorter than the time for the jet head to advance one cocoon radius,  $r_{cocoon}/v_{head}$ . The precession-driven flapping which takes place in the dynamical jet model described here is a bit slower than this. Consideration of the contact discontinuity near the head region places the effective cocoon width at the end of the simulation as half the grid width (although in reality the size of the head region varies considerably). Thus by this time the jet head has advanced roughly 5.5 cocoon radii. As mentioned above, the period of the applied precession is such that the jet has just finished 5 revolutions by the end of the run, or approximately 10 side-to-side motions. The result is that the timescale for side-to-side motions of our simulated jet is only about a factor of 2 shorter than that for the jet head to advance one cocoon radius, compared to the factor or 4 – 5 that arises from instability-induced perturbations in Norman’s model. The precession applied here is therefore “gentler” than the flapping that can arise naturally from hydrodynamic instabilities in simulations of jets similar to that modeled here.

Although jet breaking events are accompanied by extension and strengthening of a portion of the bow shock, the overall advance of the jet head is determined by the momentum flux transported down the jet, averaged over the effective working surface of the entire head region. The average advance speed of the bow shock across the grid is consistent with that predicted by Frank, Ryu, Jones, & Noriega-Crespo (1998, (equation 1)), where  $\alpha \approx \frac{1}{3} - \frac{1}{4}$  is used to approximate the averaging of the jet momentum flux over the head region to account for lateral motions of the jet. (Without averaging,  $\alpha \approx \frac{1}{6}$ .) When discussing the advance of the radio lobe, one must decide what feature, either in the dynamics or the emissions, will be used to define the lobe. Here we have chosen to consider the advance speed of the

jet head in terms of the bow shock. Since the ambient medium is uniform here, we expect the lobe advance speed to decline as the effective area of the head region increases (Cox et al. 1991; Falle 1991). The size of the computational grid used here caused the simulations to end before such longer-term jet behaviors could manifest themselves. Precession and jet breaking events cause the advance speed of the radio hotspots, when they are visible in the synthetic observations, to vary significantly.

We find that backflow velocities in excess of 30% of the initial jet velocity ( $v_b \gtrsim 25$  in simulation units) are common, sometimes reaching up to 50% of the jet speed in isolated instances (figure 1b). A reflection symmetry at  $x = 0$  might have reduced the backflow rate, however. The backflow is host to turbulence that is driven not only by fluid instabilities on the jet/backflow and cocoon/medium boundaries, but also by lateral motions of the precessing jet and especially its “flapping”. The flows are highly nonsteady. Nonetheless, velocities in the regions of strong backflow are qualitatively consistent with those estimated by the Bernoulli equation for flow between the jet head region and the cocoon in an axisymmetric source (Norman et al. 1982). Since the Bernoulli equation is a statement about steady-state flows, the application to this source is not rigorous. The qualitative agreement that we find between the backflow velocities in our model and those predicted via the Bernoulli equation may be indicative of the long-term time-averaged behavior of the cocoon. Away from the head region, the flow is typically only mildly supersonic or trans-sonic, with internal Mach numbers often less than unity. Transient strong shocks are occasionally observed in the backflow, to an extent that they can have a discernible effect on the nonthermal electron population there. This is particularly true closer to the head region where internal Mach numbers in the backflow are slightly higher, as would be predicted from a model where supersonic turbulence close to the working surface decays as the backflow passes out of the head region (Norman 1996).

Similarly fast backflows are seen in the two-dimensional simulations of JRE99. There the backflow velocities ranged over 30% – 50% of the initial jet speed along the length of the computational grid. In that case the backflow was compressed and reaccelerated through a De Laval-type nozzle, as the imposed symmetry allowed the subsonic plasma in the head region only a small channel to escape from the head into the backflow around the Mach stem. Although such channels may be temporarily disrupted during episodes of strong vortex shedding, we expect this mechanism to be much more prominent in the two-dimensional case since the Mach disk exists only at earliest times in the three-dimensional simulations presented here. While expansion and reacceleration of the flow in the cocoon may still be the origin of the supersonic backflow found in the three-dimensional case, such channels are constantly created and destroyed by the effects of precession and jet flapping.

The considerable decrease of the internal Mach number of the flow between jet and cocoon demonstrates that the plasma is strongly heated by compression in the head region, despite the absence of a persistent terminal shock. Thermal gas pressure in the head region is comparable to the momentum flux density transported down the jet, independent of whether or not a terminal shock exists. As expected, the cocoon is overpressured with respect to the jet (*e.g.*, Begelman & Cioffi 1989). While the gas pressure is generally larger near the jet head, the pressure distribution in the cocoon is quite complex (figure 2a). This reflects the violent dynamics described already. Pressure values around the head region generally approach and in some places exceed a factor of 5 over the original pressure in the jet and ambient medium. This ratio can be much higher (up to a factor of nearly 50 in one case) in small regions where the jet impinges directly on the contact discontinuity, such as after a “breaking” event. This is consistent with the expectation that the pressure just downstream of a strong terminal shock should increase by roughly the square of the internal jet Mach number, or about 64 in this case. The overpressure is not nearly as dramatic further back in the cocoon, and rarely exceeds a factor of 2 near the jet orifice.

While the jet is underpressured with respect to the cocoon, not surprisingly it is overdense with respect to the cocoon. The cocoon density does not have the same clear gradient as the pressure. The density generally varies between one-half and one-third of the jet density throughout most of the cocoon, although specific values fluctuate quite a bit from location to location. Some of these fluctuations bring the cocoon density close to the density of the jet downstream of the first oblique shock, or about 1.5 times the initial density (giving the first oblique shock a Mach number of 1.3). In a thin layer just inside the contact discontinuity, the cocoon density is typically closer to this jet value downstream of the oblique shock rather than the much lower densities found throughout the rest of the cocoon. The low density and high pressure of the cocoon contribute significantly to the overall stability of the jet. As is generally the case for heavy jets, the overdense jet propagates ballistically through the cocoon.

The temperature distribution in the cocoon is naturally also very complicated. A temperature gradient is discernible in the backflow, however, as adiabatic expansion works to cool the plasma while it flows towards the core. As expected in light of the fast backflow velocities just described, the backflow near the jet orifice has not achieved equilibrium with the ambient gas by the end of our simulation. The age of oldest material in the backflow near the orifice is only roughly half the simulation duration by the end of the simulation, as older material has already exited the grid via the open boundary. The plasma beta parameter increases significantly ( $\beta \sim 10^3 - 10^4$ ) throughout much of the cocoon, owing to the combined effects of the increased thermal pressure and the decreased magnetic fields described below. Overall we see little detailed similarity between the distributions of thermal pressure and

magnetic pressure in the cocoon plasma, as shown in the volume-rendered images of thermal and magnetic pressure in figure 2. This is expected, since the former is generally enhanced by compression, whereas shearing flows are often the cause of magnetic pressure increases, as described below.

Alfvénic Mach numbers in the jet are initially close to 70. In conjunction with the plasma beta parameter  $\beta \sim 10^2$ , this indicates that the jet magnetic field is dynamically unimportant at the outset of the calculation. Alfvénic Mach numbers within the jet itself remain steady virtually all the way to the head region, with  $\lesssim 25\%$  variations where weak oblique shocks temporarily compress the magnetic field. Thus magnetic tension has a minimal effect upon the dynamics of the jet itself throughout the calculation.

Magnetic field structures in the backflow are subjected to the same stretching and twisting effects in three dimensions as the vortex structures, so we expect to see the development of magnetic flux tube complexes as well. The resulting nonuniformity can be expressed through the magnetic field intermittency,  $I_B = \frac{\langle B^4 \rangle}{\langle B^2 \rangle^2}$  (Ryu, Jones, & Frank 2001), which can be crudely thought of as a reciprocal “filling factor”. Inside the jet lobes,  $I_B$  can approach large values  $\lesssim 100$  at late times, which indicates that the field has developed a predominantly “bundled” topology. This leads to the appearance of bright emission filaments in the cocoons of these objects when synthetic radio observations are conducted, as discussed in section 4.3 below. Such filaments are commonly observed in real radio observations (*e.g.*, M87 (Hines et al. 1989), Cygnus A (Carilli et al. 1991)) and are typically interpreted as magnetic structures. We would agree, based on our simulations.

Field-line stretching within shearing flows can quickly amplify magnetic fields, although such amplification does not appear to be sustained locally over long distances or times in the backflow. Instead, regions of the most extreme field amplification are discrete and appear briefly. (That is not to say that their effect on the spectral distribution of nonthermal particles is quite limited. We will see in section 4.3.2 that they can give rise to large islands of very strongly aged material.) Jet material downstream of the “elbow” during a jet breaking event can get sheared by the backflow, thus introducing small high-field filaments into the backflow. Such instances can bring the field strength up to dynamical importance, although these filaments quickly undergo adiabatic expansion. Once the flow becomes truly three-dimensional, the mean magnetic field varies slowly with an overall decrease by a factor of a few over the duration of the simulation. This indicates that large-scale field amplification such as that from a precession-driven turbulent dynamo is not taking place. We would not expect a dynamo-driven amplification of the large-scale fields, despite the apparent introduction of a net helicity via precession. In fact it is important to point out that precession adds little or no net helicity at all to the problem, since in the absence of interactions with



the backflow, all jet material moves in a straight line from the orifice. Compression of the field where the beam splashes against the contact discontinuity is another cause of transient field growth.

The absence of axisymmetry-enhanced vortical rings in the three-dimensional calculations results in a greatly lessened tendency towards “flux expulsion” (Weiss 1966); that is, the annihilation of poloidal field components driven by reconnection. Nevertheless large volumes of the cocoon are host to magnetic pressure values greatly diminished below the nominal value transported down the jet, often by two orders of magnitude or more. This is consistent with the observation by Clarke (1996) that weak lobe magnetic fields are typified by extended filamentary structures and large magnetic voids. This is also consistent with the large values of  $I_B$  mentioned above. Adiabatic expansion is the primary engine for this field reduction. These large regions may act as “freezers”, tending to preserve particle spectra against continuous radiative aging (Scheuer 1989; Eilek et al. 1997), if the energetic particles remain in these volumes for long periods of time (Blundell & Rawlings 2000).

The diminishment of magnetic fields in the cocoon also drives the Alfvénic Mach number,  $M_A = u/v_A$ , up by an order of magnitude over its original value in the jet,  $M_{Aj} \approx 70$ , signifying that the plasma kinetic energy density exceeds the magnetic energy density and that magnetic tension is dynamically unimportant in these volumes. However the magnetic filaments described above occasionally correspond to  $M_A \lesssim 10$ , which is nearly an order of magnitude less than the original jet value. The dissolution of these filaments is partially mitigated by the resident fields, although the Alfvénic Mach number rarely becomes much smaller than 10. In contrast, JRE99 found many locations in their analogous axisymmetric models where  $M_A \lesssim 1$ . There the flows were made smoother by the presence of the field, via reorganization and realignment of the flow after reconnection events.

One must use caution while interpreting detailed magnetic field properties in these or any such simulations. First, there are fundamental differences expected between axisymmetric field evolution and fully three-dimensional fields. For an axisymmetric field the  $B_\phi$  component is partially decoupled from  $B_r$  and  $B_z$ , so is not subject to reconnection. On the other hand  $B_\phi$  can be strongly enhanced by flux stretching if a plasma element expands in the radial direction. Thus  $B_\phi$  tends to become dominant in axisymmetric MHD simulations. That effect is largely gone in three-dimensional flows that are disordered, since all components participate in the reconnection. On the other hand flux tubes in 3D tend to be stretched and twisted, so can become locally strengthened beyond two-dimensional flows (see, *e.g.*, Ryu et al. 2001). At the same time these effects are limited by finite numerical resolution, so simulations are not able to establish accurately the smallest values of  $B$  or  $M_A$  that would be expected to occur locally. We are confident, however, that the global

properties of the cocoon fields seen in these simulations are correct.

A similar comment holds regarding magnetic reconnection in these simulations. The dissipative effects which give rise to reconnection here are purely numerical in origin, and thus not representative of the microphysics that governs such transitions in the real world. These simulations are, therefore, unable to provide information about the local rate of reconnection or the role of reconnection in heating the plasma in radio galaxy lobes. Since reconnection is basically a topological transition, however, its presence in the complicated magnetic field configurations found in our simulated sources is reasonable (*cf.* Ryu et al. 2001).

## 4.2. Electron Transport

We now turn to a consideration of the electron transport effects within each model. The cosmic-ray electrons in these simulations are dynamically passive, and in fact as a consistency check we note that their nominal energy density never exceeds more than 0.1% of the kinetic energy density anywhere in the computational grid. Because the electron transport takes place “on top” of the dynamics, the fact that the three models outlined here are dynamically identical enables us to examine in a straightforward way the means in which various momentum-transport effects can alter electron populations subjected to the same dynamical history.

### 4.2.1. “Adiabatic” Models 1 and 2

The absence of radiative cooling and injection effects in model 1 make it the most straightforward to analyze. Nevertheless the nonthermal particle populations in this simplest model deserve close scrutiny.

As stated previously, nonthermal electrons in this model enter the grid via the jet orifice. The negligible radiative cooling rate in this model ensures that the particles are transported down the jet with momentum indices virtually unchanged, and the distribution of magnetic fields is largely immaterial to this discussion. Thus they enter the shock-web complex as a uniform power-law momentum distribution with index  $q = 4.4$  before passing from the jet itself into the cocoon. The oblique shocks along the jet are too weak to modify the electron population in this model.

Recognizing the role of the shock-web complex is crucial to understanding how the dynamics of these simulated sources affects the nonthermal electron transport and in particular the distribution of momentum indices in the cocoon. All material that enters the cocoon

does so only after passing through the diaphanous shock web, which may mean passing through a strong shock, passing through a weak shock, or flowing through a “hole” where no shock is found. In any case the shock web makes an indelible impression upon the manner in which the particle transport properties manifest themselves in the cocoon, because even in the control model (model 1) it allows a subtle variety of particle spectra to enter the cocoon.

In model 1, the only momentum transport effect to which the particles in the shock web may be subjected is a flattening at sufficiently strong shocks. Thus only downstream of relatively strong (and therefore somewhat rare) shocks with compression ratio  $r \gtrsim 3.14$  will the particle momentum index differ from 4.4. Another way to express this is in terms of the shock Mach number, which must exceed  $M = \sqrt{q/(q-4)}$  to reaccelerate particles with momentum index  $q$ , and thus requires  $M \gtrsim 3.3$  to flatten a distribution with  $q = 4.4$ . Recall that in many places in the cocoon, the internal Mach number is often less than unity. Since there often is no terminal shock, and since when it does exist it is often weaker than  $M \approx 3.3$ , most of the jet material enters the cocoon without being flattened. Small amounts of flatter material are sporadically introduced into the cocoon, at times and places where a portion of the flow passes through a sufficiently strong shock. Considerable variety is seen even in these strong shocks, so these small amounts of shock-accelerated material enter the cocoon with an unpredictable variety of momentum indices less than 4.4. Thus we see mostly momentum indices of 4.4 in the cocoon, with small ribbons of flatter material downstream of strong shocks. The fact that we see spectral structure, even in the control model, serves as a reminder that by looking at momentum indices we are not seeing a snapshot of the dynamical state of the system so much as we are seeing information about the dynamical history of the nonthermal particles.

In the injection model (model 2) as in model 1, it is predominantly through the action of the shock web that the simulated dynamics affect the relativistic particle transport. Again the variation of magnetic field strengths throughout the simulated source is essentially unimportant to the electron population because of the extremely low radiative cooling rate in this model. Yet the inclusion of fresh particle injection at shocks makes a profound difference. We found in the control model that basically only the strongest shocks in the shock web influenced the particle transport and that the spatial and temporal intermittency of such shocks limited their influence greatly. As before, in model 2 the momentum indices flatter than the original jet value of  $q = 4.4$  are only found downstream of the strongest shocks. Yet unlike model 1, most of the nonthermal electrons in this simulation are introduced at shocks rather than at the jet orifice. Thus, now all of the shocks in the shock web, weak and strong alike, contribute. In fact it is the weak shocks ( $r < 3.14$ ,  $q > 4.4$ ) that take center stage in this model. Since internal Mach numbers in the backflow are often only mildly supersonic as described above, weak shocks outnumber the relatively strong shocks, ensuring that more

steep-spectrum material enters the cocoon than flat-spectrum material. This is particularly true at times corresponding with a “jet breaking” event, when the shock web is especially complex and spread over the entire head region. This is demonstrated in figure 3a. There we see predominantly more steep material in the jet head (reflecting local injection by weak shocks) than further back in the cocoon, near the jet orifice (reflecting the stronger shocks formed early when the jet flow was almost two-dimensional).

#### 4.2.2. “Cooling” Model 3

When radiative aging becomes significant, the distribution of magnetic field strengths throughout the simulated flow is no longer immaterial to a discussion of the electron transport. Thus in addition to the action of the shock web, the magnetic fields provide a second crucial link between the source dynamics and the particle transport in model 3.

The shock web plays more or less the same role here as it did in the control model (model 1), with a slight difference. Once again all of the nonthermal particles enter the grid via the jet, but now radiative aging is significant enough in this model that the relativistic electrons propagating down the jet exhibit a modest amount of spectral curvature by the time they encounter the shock web. Sufficiently strong shocks will reaccelerate the curved distributions into power laws before they pass into the cocoon. Yet as before a large fraction of the material coming down the jet passes through weak shocks, or indeed no shock at all, before entering the cocoon. Not only does the jet itself steepen noticeably between orifice and the terminal shock, which does exist at this time, but the lack of fresh-particle injection in this model means that there is a paucity of flat-spectrum electrons at the post-shock location. In the injection model, there was a significantly flatter population downstream of the terminal shock, but not here. Most particles enter the cocoon without the benefit of strong shock acceleration. Thus in contrast to models 1 and 2, we now see the introduction of non-power-law distributions into the cocoon even before radiative cooling can take place in that complicated magnetic environment.

As described above in section 4.1, large volumes of the cocoon are occupied by “freezers”, where the magnetic pressure drops significantly below the inflowing jet values. The radiative lifetime of nonthermal particles at the fiducial momentum inside these volumes exceeds the nominal lifetime by more than two orders of magnitude. Regions of rapid cooling are restricted to a smaller fraction of the cocoon volume, in the form of the high magnetic field filaments that are generated by shearing flows at the jet head, and that thread the larger magnetic voids. The extreme variability of the cocoon magnetic field, both spatially and temporally, makes the creation of these strong-cooling regions sporadic. Often we see

different regions within the same source between which the effective cooling rate can vary by orders of magnitude. We note however, that this would not necessarily be the case if the calculation were performed at a higher redshift. As noted above, the  $(1+z)^{-4}$  dependence of the nominal cooling rate  $\tau_{s0}$  means that inverse-Compton losses become significant at high redshift even when the relevant magnetic fields are weak. In model 3, the cooling contribution from inverse-Compton losses would equal the contribution from synchrotron losses in the fiducial field ( $5.7\mu\text{G}$ ) at a redshift of only  $z = 0.16$ . Inverse-Compton losses would therefore dominate cooling in the magnetic voids at even lower redshifts.

The effects of radiative aging on the distribution of momentum indices in the source is seen in figure 3b. Also clearly visible in this figure are dark channels representing regions where ambient material has been entrained into the jet cocoon. This illustrates the Kelvin-Helmholtz unstable character of the cocoon boundary, which leads at later times to mixing between the arbitrarily steeper ambient population and the flatter jet populations.

### 4.3. Synthetic Observations

Our goal here is to develop an understanding of the connections between physical structures and observable emission patterns present in these simulations, with eventual application to real radio galaxies. We emphasize, however, that the current simulations are still intentionally idealized to allow the best isolation of clear cause and effect relationships. We utilized the combined vector magnetic field structure and nonthermal particle distributions within the simulations to compute a large set of synthetic observations of our simulated radio galaxies. By synthetically observing a source whose detailed physical structure is known beforehand, we hope to gain insights into what real observations are reliably telling us. The simulated objects represent truly three-dimensional objects with a self-consistent particle energy distribution, so these synthetic observations are a big step beyond previous calculations of this type.

In every zone of the computational grid we compute a synchrotron emissivity (JRE99; Jones, O’Dell, & Stein 1974)

$$j_\nu = j_{\alpha 0} \frac{4\pi e^2}{c} f(p) p^q \left( \frac{\nu_{B_\perp}}{\nu} \right)^\alpha \nu_{B_\perp} \quad (3)$$

where  $\alpha = (q - 3)/2$ ;  $j_{\alpha 0}$ , a function of  $\alpha$ , is of order 1 (Jones et al. 1974); and  $\nu_{B_\perp} = \nu_B \cos \theta$ , the electron cyclotron frequency in terms of the magnetic field projected on the sky plane, with  $\nu_B = eB/2\pi m_e c$ . The distribution  $f(p)$  and  $q$  are found by equating a selected observational frequency  $\nu$  to the critical synchrotron frequency of emission,  $\nu_c$ , to identify a momentum  $p = m_e c [2\nu_c/(3\nu_{B_\perp})]^{(1/2)}$ . This calculation is performed in the

rest frame of the simulated radio galaxy, with the appropriate redshift correction made for the observation frame. It also explicitly takes into account variations in the angle of the magnetic field projected on the plane of the sky,  $\theta$ . For these simulations all flow speeds are subrelativistic, so kinematic Doppler factors and light-travel times are ignored. Note that because we are explicitly calculating the momentum distribution of nonthermal electrons in the simulations, we obtain a local slope to the momentum distribution,  $q$ , by interpolating between momentum bin centers. The synchrotron spectral index  $\alpha = (q - 3)/2$  obtained from these synthetic observations is therefore self-consistent. Previously, spectral indices in synthetic observations from purely MHD simulations had to be included in an ad hoc fashion (Matthews & Scheuer 1990a; Clarke 1993). Surface brightness maps for the optically thin emission are produced from our emissivity distributions via raytracing through the computational grid to perform line-of-sight integrations, thereby projecting the source on the plane of the sky at any arbitrary orientation. This method also enables us to compute Stokes parameters for the synchrotron emission (Clarke et al. 1989), as well as the correction for Faraday rotation through the source, making detailed polarimetric studies possible. We have also produced X-ray surface brightness maps in the same fashion, by calculating the inverse-Compton (IC) emissivity from the interaction between the cosmic microwave background radiation and the nonthermal electrons (Tregillis, Jones, Ryu, & Park 2001b).

The synthetic observations can be imported into any standard image analysis package and subsequently analyzed like real observations. The analysis here was performed using both the MIRIAD and KARMA (Gooch 1995) packages. For example, it is a straightforward matter to construct spectral-index maps from a set of observations over a range of frequencies. To make this exercise as realistic as possible we place the simulated object at an appropriate luminosity distance, set to 100 Mpc for the observations included here, although that choice has no influence on our conclusions. Because our primary interest here is in identifying general trends, the observations are presented at their full resolution with very high dynamic range, although it is straightforward to convolve the images down to lower resolution before making comparisons to true observations. We note that line-of-sight integrations generally tend to enhance regions of flatter emission over steeper emission, and suppress regions of weaker emission. Therefore when investigating our three-dimensional sources we have been careful to study multiple orientations in order to identify accidents of projection along the line of sight.

The radio luminosity of our simulated sources is somewhat arbitrary, as it scales with the ratio of nonthermal to thermal particle number densities in the jet,  $\delta$ . This is essentially a free parameter in the simulations as long as the energy density in nonthermal electrons remains dynamically unimportant. As a consistency check, we compute the spectral luminosity  $L_\nu$  at 1.4 GHz and compare this value to the jet kinetic luminosity,  $L_j$ . In all cases we find  $L_\nu$

to be significantly less than the kinetic luminosity. For the time corresponding to that in the images ( $t = 4.0$ ), we find  $L_\nu/L_j = 4.9 \times 10^{-10} \times (10^4 \delta)$  for model 1,  $3.7 \times 10^{-10} \times (10^8 \delta)$  for model 2, and  $4.0 \times 10^{-7} \times (10^4 \delta)$  for model 3. (Recall  $\delta = 10^{-4}$  in models 1 and 3, and  $\delta = 10^{-8}$  in model 2.) We find the highest ratio in the model with the strongest magnetic fields (model 3), and the lowest ratio in the model with the lowest cosmic ray number densities (model 2). Note that these are the models expected to have the highest and lowest radio luminosities, respectively. The jets are still too dynamically young by the end of the simulations to have undergone any significant luminosity evolution.

#### 4.3.1. “Adiabatic” Models 1 and 2

Figure 4 shows an image of synthetic synchrotron surface brightness at 1.4 GHz for  $t = 4.0$  in model 1. Figures 5a and b show the corresponding image for model 2 and the two-point spectral index computed from maps at 1.4 GHz and 5.2 GHz for  $t = 4.0$  in model 2, respectively. The orientation of the source in these images corresponds approximately to that of the computational volume in the volume rendered images. In both cases we have restricted the calculation of synchrotron emissivity only to regions where the jet color tracer  $C_j \geq 0.99$ . Since  $C_j = 0$  in the ambient medium, this selects emission originating only from material that entered the computational volume by way of the jet.

The jet and its cocoon are both readily visible in each of the surface-brightness images. The bright ellipse at the lower-right is the orifice where the jet enters the computational grid. Faint brightness enhancements are visible in the radio jets of both models, the smallest of these also being the most prominent. We find that the enhancements are caused by the very slight increase in the jet magnetic field at the oblique shocks, such as the conical oblique shock which is faintly visible just downstream of the jet orifice in figures 4 and 5a. Another such enhancement can be made out roughly halfway along the jet in these figures, along the segment of the jet oriented nearly horizontally with respect to the page. It is reasonable to ask if these brightness variations are augmented by enhanced particle populations downstream of oblique shocks in the injection model (recall that injection of fresh particles was allowed to take place in model 2). Oblique shocks with compression ratio  $r < 3.14$  would inject particles with  $q > q_{jet} = 4.4$  into the jet flow. Only one tiny enhancement has a corresponding feature in the spectral-index map, so we conclude that acceleration at these shocks does not contribute a significant enough electron population to have much influence on the synchrotron emission.

Away from these enhancements the jet itself is of comparable surface brightness to the cocoon in model 2, yet the jet clearly dominates over the cocoon emission in model 1. In

the latter model, the entire particle population enters the grid via the jet, making the jet a relatively abundant source of emitting particles. On the other hand, the initial jet particle population in model 2 was much smaller, so the majority of emitting particles were injected freshly at shocks. Relative jet brightness is also artificially enhanced in all of our models by the dimensions of our computational box. Here, the line-of-sight length ratio between jet and lobe material is a factor of 10 at best, whereas in real radio galaxies this ratio is likely much larger.

The jet is only slightly brighter in the head region of model 1 than it is elsewhere, and comparable to the brightness near oblique shocks within the jet. There does appear to be a hotspot at the jet terminus, but it is not very prominent. In fact there is a fairly strong terminal shock at the end of the jet at this time, but it is not apparent in the synthetic image. We have found that radio hotspots in synthetic observations of these simulations do not always correspond to the spatial location of the termination shock and vice-versa (Tregillis, Jones, Ryu, & Park 2011b). The brightness increase resulting from compression of the magnetic field and the local electron population at the terminal shock does not outstrip that at oblique shocks. Thus from the viewpoint of the observed emissions, there is little practical difference between the structure at the end of the jet and the oblique shocks further upstream at this time in the simulation.

Such is not the case in the injection model. The hotspot complex in model 2 consists of a compact, bright region apparently associated with the termination of the jet, connected by a thin bridge of emission to a larger region of enhanced brightness. We will follow convention and refer to the smaller, brighter region as the “primary” hotspot, and the larger, weaker region as the “secondary” hotspot. The advantages of combining synthetic observations with the known dynamical history of a simulated source become apparent as we investigate the nature of these hotspots.

Notice how the secondary hotspot is elongated in a direction roughly parallel to the outer cocoon wall, and normal to the line leading to the primary. This very nicely fits the description of a “splatter spot” (*e.g.*, Williams & Gull 1985; Cox et al. 1991). In the splatter spot scenario, there is an outflow from the primary hotspot that impinges upon the opposite wall of the cocoon, providing an energy supply for a secondary hotspot. The notion of a primary outflow appears to be an apt description of the flow dynamics inferred solely from this single synthetic observation. It leads us to interpret the bridge as a flow which connects the primary and secondary hotspots. However, since there are other possibilities (for instance, the apparent relationship between the primary and secondary may only be an accident of projection) it is difficult to know if this interpretation is correct without further information.



More direct evidence that the secondary hotspot in figure 5a is the result of an outflow from the primary hotspot is obtained by considering the jet dynamics. Analysis reveals that the jet is undergoing a “breaking” event as described above in section 4.1. The highest velocity core of the jet is severely bent, and the primary hotspot here is in fact associated with the shock at the “elbow”. The synchrotron emissivity jumps by over four orders of magnitude across this shock, going from the faint jet to the bright hotspot. Close inspection of the behavior of the magnetic pressure in the same region reveals an increase only by a factor of  $\approx 2.6$ . On the other hand, injection of fresh energetic particles from the thermal plasma passing through this shock increases the population of particles in the momentum bin of interest by a factor of  $\approx 1.1 \times 10^4$  since a very minimal population was present in the jet at the beginning. Thus, the brightness of the primary hotspot is almost entirely the result of an enhanced particle population at the shock and not a dramatic increase in magnetic field strength. The newly-injected electrons flow through the bridge into the secondary hotspot, where the magnetic pressure increase over the jet value is still  $\lesssim 3$ . This outflow from the primary hotspot is key to the appearance of the secondary hotspot.

We note here that multiple hotspots are not uncommon in synthetic observations of the injection model, yet not all secondary hotspots are splatter spots. Another model for secondary hotspots is the so-called “dentist’s drill” model (Scheuer 1982). In this case the jet impinges upon the cocoon wall upstream of a primary hotspot, forming a new primary hotspot while the old primary subsequently appears as a secondary hotspot. This is distinguished from a splatter spot in that the secondary is not powered by an outflow directly from the primary. Such a situation occurs at  $t=3.6$  in the simulation. Lacking any power supply at all, such a disconnected hotspot might be expected to dissipate on a timescale on the order of its adiabatic expansion time (Valtaoja 1984; Lonsdale & Barthel 1986). Our findings support those of Cox et al. (1991), who find that such secondaries may last considerably longer than this. Rather than being downstream of an outflow directly from the primary hotspot, they may be powered by material that was downstream of the “elbow” during a jet “breaking” event as described in section 4.1. Dissipation occurs not on the adiabatic expansion timescale but on the order of the time it takes the disconnected material near the jet head to reach the secondary.

We find that the advance speed of the terminal shock (when such can be easily identified) varies by a factor of several around the mean velocity determined by the total time required to traverse the grid. As mentioned above, there is not always a one-to-one correspondence between hotspots and terminal shocks in these synthetic observations. Nonetheless the highest-velocity fluctuations correspond to the “breaking” events described above when the newly realigned jet head surges forward. Often the jet has a strong, transient terminal shock and a bright hotspot during these events.

The jet in these models has a spectral index of  $\alpha \approx 0.7$ , as expected for  $q_{jet} = 4.4$ . Both models also show spectra flatter than 0.7 at the primary hotspot, which again is as expected if the hotspots are identified as the location of a strong shock. Yet the absence of radiative cooling in these adiabatic models leads to cocoon spectral index distributions that at first glance may seem to be at odds with the paradigm for radio galaxy spectra.

For model 1, the cocoon spectral index is extremely uniform, and shows only very minor variations ( $\Delta\alpha \approx 0.01$ ) from the jet value, with the cocoon only marginally steeper than the hotspot. As described in section 4.2.1, only small amounts of material with  $q < 4.4$  (corresponding to  $\alpha < 0.7$ ) enter the cocoon in model 1. All of the material in the cocoon is subjected to adiabatic expansion. The effect is to shift the observed spectrum by equal amounts in  $\log I$  and  $\log \nu$  (Katz-Stone & Rudnick 1997). For a pure power-law spectrum this introduces no curvature when observing a source at a fixed frequency. This is in contrast to what was found in the analogous model 1 in JRE99. There much of the emission outside of the jet, including the brightest parts of the cocoon, was associated with spectral indices flatter than the  $\alpha = 0.7$  within the jet itself. Because the nonthermal particle spectra are essentially still power laws, the flow of material into the adiabatically-expanded magnetic voids does not lead to increased spectral curvature in the observed emissions.

For model 2, we find the steepest spectrum material near the head of the cocoon, and the spectral index of the cocoon actually flattens towards the jet origin, which is completely at odds with what would be expected based on the standard paradigm for radio galaxy aging. We found in section 4.2.1 that the weaker but extensive elements of the shock web inject large populations of steep-spectrum electrons into the cocoon in model 2. Just downstream of these weak shocks, emission from these freshly-injected steep populations can dominate over the unmodified jet material because the population transported down the jet is small in this case. This leads to the appearance of flat-spectrum hotspots as islands in a sea of much steeper emission. The secondary is slightly steeper than the primary because of adiabatic expansion.

Two effects cause the lobe radio emission in this model to become flatter as material moves out of the head region. As the newly-injected steep-spectrum material joins the backflow, it mixes with older, flatter material (that has either been reaccelerated or injected at a previously existing strong shock or has passed directly from the flatter jet into the backflow) causing the overall cocoon emission to quickly flatten out as it moves back toward the core. Secondly, as has been mentioned above, the magnetic field in the cocoon is generally weak owing to adiabatic expansion into the lobe. Lower magnetic field values select higher-energy electrons at a given observation frequency, which typically results in steeper emission for convex spectra, such as those obtained from radiative aging of an initially power-law

distribution. However, analysis of color-color diagrams (as per Katz-Stone & Rudnick 1997) of these data reveals the cocoon spectra to be concave in the injection-dominated case of model 2, as expected. (Recall the absence of radiative cooling in this simulation.) Thus, the higher-energy electron populations selected by the diminished lobe fields are actually flatter than the lower-energy populations. This also contributes to the flattening of the lobe spectrum as material moves out of the head region.

It is important to point out here that the presence of both steep- and flat-spectrum populations along the same line of sight can have a dramatic effect upon the resulting spectral-index maps. For a given magnetic field and nonthermal particle number density, flatter-spectrum populations are more likely to dominate the emission over steeper populations, especially at higher frequencies. Nevertheless, while the steep emission around the jet head varies in prominence as the orientation of the source on the sky is varied, the general trend does not disappear. Rather than being an artifact of orientation, this trend is a property of the model throughout the length of the simulation after the disruption of the Mach disk.

This differs from what was seen in the analogous axisymmetric model in JRE99. There, the general trend was for steepening away from the jet head, in accord with the usual expectations for radio galaxy spectra. In that case, the enforced symmetry prevents the creation of a shock web complex capable of generating the prodigious amounts of steep-spectrum material needed to dominate emission over the flatter jet material. The shock web is simply a consequence of broken symmetry in the three-dimensional calculation, and the “backwards” spectral index gradient is simply a consequence of the injection-dominated particle transport taking place within the shocks of modest strengths within the web. This model represents an extreme idealized case where injection of fresh particles at shocks dominates the non-thermal particle transport, and as such is not meant to represent a real-world radio galaxy. (However Treichel et al. (2001) have found that spectral analysis of the FR II radio galaxy 3C 438 reveals steeper emission near the head than closer to the core.) A real radio source characterized by these dynamical and transport effects would exhibit this kind of spectral index gradient. The existence of such clear features in one model does bring out the diagnostic potentials for exploiting the relative importance of local electron injection in weak shocks associated with backflows.

#### 4.3.2. “Radiatively Aged” Model 3

Figures 6a and 6b show images of synthetic surface brightness at 1.4 GHz and the synchrotron spectral index computed from maps at 1.4 GHz and 5.2 GHz for  $t = 4.0$  in

model 3. The source orientation in these figures is identical to that in figures 4 and 5. As above we have restricted the emissivity calculation to jet material only ( $C_j \geq 0.99$ ), but we have also restricted the calculation to zones where  $q \leq 8$  ( $\alpha \leq 2.5$ ). This condition is a reasonable way to avoid occasional spurious numerical effects arising close to electron cutoffs, since extremely steep populations would likely be weak emitters anyway, and results in the exclusion of only a small number of zones.

Again we find the jet core dominates the source for the same reasons as explained in section 4.3.1. Since in this model new energetic particles are not being introduced into the flow at shocks, the brightness variations are largely tracers of magnetic field enhancement, as in model 1. Thus we see the familiar pattern of brightness increases near oblique shocks in the jet, without corresponding features in the spectral index map. There is also a dramatic variation of surface brightness throughout the cocoon, where high-surface-brightness filaments wind through fainter material.

The key effect that differentiates between brightness maps of models 1 and 3 is the mixing along lines of sight between flatter and steeper (radiatively aged) populations. Since this mixing will tend to emphasize the former, we expect to see more similarities between the surface brightness maps of models 1 and 3 beyond those expected on the basis of the identical dynamics in those two models. And indeed, while the jet and cocoon are both readily visible as in models 1 and 2, the jet terminal structure is much more akin to that of model 1 than the hotspot complex of model 2. In fact the jet terminus associated with the primary hotspot in model 2 exhibits only a very minor brightness enhancement beyond the overall brightness of the jet, and the region corresponding to the secondary hotspot is much diminished in intensity. Again we emphasize the fact that these simulations are dynamically identical, and thus the jet terminus does host a strong terminal shock at this time in model 3 as well. A tiny “sliver” of material can be seen flowing out of the terminal shock region, along the lower edge of the contact discontinuity, without suffering even the mild brightness enhancement associated with the shock in this model. This flow element is not prominent in model 2 as it represents material that passed from the jet into the cocoon without being shocked, but it is also visible in model 1.

While the surface brightness distribution is similar to that of the control model, the spectral index map differs substantially. The jet itself has aged noticeably, steepening from  $\alpha_{jet} = 0.7$  to  $\alpha \approx 0.8$  just prior to the primary hotspot. The jet does appear to experience appropriately stronger cooling in the stronger magnetic field near the primary hotspot, with  $\alpha \gtrsim 1$  there. Virtually all of the cocoon material is steeper yet, with  $\alpha \approx 1.0 - 2.0$ . The distribution of indices strongly suggests almost random mixing between the steepest and flattest regions rather than a clear gradient away from the jet head as in model 2. In fact,

close inspection of the spectral index map near the primary hotspot clearly shows the same tiny sliver of jet material mentioned above, which flows past the primary into the secondary hotspot without suffering the aggravated cooling experienced by most electrons in this region. Again we see the result of highly complex flow patterns in and around the jet head, this time allowing small amounts of material to escape aging in the high field regions associated with a hotspot, thereby injecting comparatively “young” material into the cocoon. Strong mixing between this material and material that has been processed through the high-field regions of previous hotspots and filaments in the backflow is the source of this complex spectral index pattern.

Also, these simulated sources are fairly young in terms of their dynamical histories, so individual events (*e.g.*, breaking of the jet) in their evolution can still have strong effects on the overall appearance of the source. The moderately steep region in the upper-center part of the spectral index map (above the jet) for this model is the result of a single, brief and strong magnetic field enhancement owing to shearing at the jet end at an earlier time in the source evolution. As explained in section 4.2.3, the source dynamics leads to sporadic creation of strong-cooling regions and large magnetic “voids”. The lower fields of the voids lead to emission from higher-energy particles (for a given observation frequency), and thus emphasize the cooling-induced spectral curvature in this model. If the flows conspire to keep large numbers of particles in these volumes for significant lengths of time, the overall aging rate could be much slower than would be estimated based on regions of high emissivity, where the fields are often stronger than average.

Unlike the previous models 1 and 2, the hotspots here in model 3 do not correspond to significantly flatter spectra. As explained in section 4.2.3, radiative aging of material transported down the jet and the lack of fresh particle injection at the relatively rare strong shocks are contributing factors. Here synchrotron cooling in the moderately enhanced magnetic field of the hotspot has overcome reacceleration at the cospatial strong shock. On top of mixing this exacerbates the difficulty in finding a spectral gradient away from the jet head region. This contrasts with what might have been expected based on the analogous axisymmetric model (JRE99), where the terminal shock and indeed the oblique shocks within the jet flattened the jet material, even in their strong-cooling simulation. This is possible in the axisymmetric model because there as here the jet spectrum undergoes some radiative aging between the orifice and the terminal shock, but there the oblique shocks are just strong enough to reaccelerate the slightly-aged jet material. While still highly variable the terminal shock in the axisymmetric simulations is generally stronger than those in the shock web complex here.

In model 1 there were hardly any spectral index variations in the cocoon to correlate

with brightness variations. Here, however, there is in general a nice correlation between brightness and spectral index, in the sense that brighter material is typically flatter than surrounding fainter material. This relationship is not so clear-cut in model 2, where the hotspots are certainly flat, yet the prevalence of steep-spectrum emission from the region around the jet head resulting from substantial electron injection at weak shocks does not appear to lead to a diminished brightness compared to other parts of the cocoon.

#### 4.3.3. *General Comments: Electron Transport and RG Dynamics Application to Real Radio Galaxies*

In each of the models considered in the previous sections the cocoon appears to have an intricate network of bright filamentary structures spread throughout material of lower surface brightness. The magnetic intermittency ( $\frac{\langle B^4 \rangle}{\langle B^2 \rangle^2}$ ) calculated for the entire cocoon volume at this time is approximately 100, indicating that the magnetic field structure is also extremely filamentary. Most high magnetic field regions outside of the jet core are confined to a relatively small volume of flux tubes that wind through the source. Application of “spectral tomography” techniques (Katz-Stone & Rudnick 1997) to these data reveal no readily-apparent overall structure in the cocoon filaments, although there is a wealth of fine structure in both surface brightness and the spatial distribution of various spectral indices.

In 1989, Scheuer put forth some simple but compelling arguments that adiabatic compression of the magnetic field alone could increase hotspot brightnesses by even 2 orders of magnitude over the jet, and that in fact it is almost surprising that jets can be seen at all. Model 1 presented here is most similar to the situation considered for these arguments. Even there, however, we see a jet very much brighter than the cocoon, roughly ten times so at the time shown in the figures. We find that the various shocks in the complex near the jet head rarely compress the field to such a great extent, even when they are strong. Rather, shearing of the flow near the end of the severely-bent jet is the leading creator of the filamentary strong-field regions in the backflow. As has been pointed out above, in these models adiabatic expansion into the lobe acts to reduce the brightness of the cocoon. The issue here is the question of field compression in the terminal shock, which is often weak and hard to identify. This reminds us that the working surface in these models is not just the terminal shock.

By restricting the emissivity calculations here to the volume inside the contact discontinuity (where  $C_j = 1$ ), we have ignored emission arising from shocked ambient medium. Yet it is interesting to note that even when the effective area of the working surface of the jet head is augmented by the time-averaged effects of precession, the thermal plasma flux

through the bow shock in the ambient medium may still be larger than the analogous flux through other shocks in the system. Significant nonthermal emission might therefore arise from shocked ambient medium between the jet contact discontinuity and the bow shock if the magnetic field there is strong enough. Particularly in our injection-dominated model 2, we see a considerable amount of emission in the ambient medium, when it is not excluded. This emission evidences variations along the length of the source consistent with irregular cycles of weakening and strengthening of the bow shock. Naturally this emission depends strongly on the character of the ambient magnetic field, and it is difficult to know in detail how a different treatment of this field in our models would alter the effect. Note, however, that there is mounting evidence that magnetic fields in some clusters may approach  $10\mu\text{G}$  (*e.g.*, Clarke et al. 2000), yet in at least one very powerful source, Cygnus A, the bow shock has been reported to be radio quiet (Carilli et al. 1988). If this is generally true, then we may in the future be able to place constraints on conditions in the ambient medium and properties of the jet plasma. Doing so would require a more realistic model for the magnetic field in the ambient medium as well as in the jet itself.

## 5. CONCLUSIONS

We have applied the nonthermal particle transport scheme developed by JRE99 to the study of three-dimensional MHD flows, in an attempt to gain insights into the way that the large-scale dynamical processes in radio galaxies affect the relativistic electron populations that reside within. We have examined the role of adiabatic cooling, radiative cooling, and first-order Fermi acceleration and injection of fresh particles at shocks. In order to illustrate better the connection between the flow dynamics and the relativistic electrons, we have introduced a set of synthetic observations that for the first time compute an approximate synchrotron emissivity directly from the local magnetic field and nonthermal particle distributions. This work is an extension of the axisymmetric studies cited above. The most important and striking new findings are listed below.

1. The spatial and temporal shock structure associated with the jet head in these studies is extraordinarily complex. The notion of a single, simple, strong terminal shock is applicable only rarely after the flow has begun to assert its true multidimensional nature. This has profound consequences for the electron populations processed through these shocks and also for the associated synchrotron radiation. This cautionary note applies not only to sources that display strong evidence for precession, but virtually any sources with complex morphologies. Our precessed jets show evidence for episodic reappearance of a transient strong terminal shock and subsequent sudden advances of the jet head. The complexity

of driven multidimensional flows (Sato & The Complexity Simulation Group 1996) makes similarly complicated effects in other scenarios quite likely.

2. This so-called “shock-web complex” may lead to spectral distributions that confound interpretation in terms of the standard model for radio galaxy “spectral” aging. In the case of injection, this may occur by way of introducing a significant population of steep-spectrum particles on timescales that would not admit such steepening via radiative processes. Even in situations where radiative cooling effects are not negligible, a shock web may complicate interpretations by allowing radiatively-aged electron populations to flow from the jet directly into the backflow without getting reaccelerated at a shock, even inside a hotspot; conversely, it may allow jet material to escape from a hotspot without being subjected to the strong magnetic field there. All of this underlines the fact that the emissions we observe from real radio galaxies yield information about not just the current state of the nonthermal particles, but also about their dynamical histories.

3. The cocoons of these sources are threaded by strong-magnetic-field filaments, but most of the volume is occupied by field values that are greatly diminished below the nominal values in the jet. While compression and shearing can enhance the local magnetic field, adiabatic expansion into the lobe with subsequent reduction in field strength appears to be the dominant effect. Such large, low-field volumes further tend to confuse spectral-aging analyses by extending the nominal radiative lifetime of nonthermal particles beyond what would be inferred based on regions of high emissivity, which mostly represent places where the fields are strongest.

4. Overall, the elaborate dynamical behaviors in these models make the detailed histories of the nonthermal particles very difficult to capture succinctly in broad generalizations. We found that even in the adiabatic control model (model 1), the energetic electrons in the cocoon do not share the same history of shock acceleration. Yet when fresh particle injection at shocks dominates the nonthermal transport (model 2), we cannot even simplify matters by restricting our attention to only the strongest shocks. Similarly, fitful amplification of the magnetic field leads to varying histories of radiative energy loss among energetic electrons in the cooling model (model 3).

We have restricted our attention here to the some of most general and wide-ranging issues, intending to lay the groundwork for further, more in-depth examinations. Later papers will apply the tools and methods shown here to more specific and detailed questions regarding the nature of radio galaxies. The insights gained from these idealized, extreme cases for nonthermal particle transport will be valuable in studies that generalize the transport model and aim to identify physical behaviors seen in specific observed objects. This first pass has demonstrated the power and necessity of explicitly modeling energetic particle



transport effects in bulk flows in any attempt to convert dynamics to nonthermal emissions.

The work by T.W.J. and I.L.T. was supported by the NSF under grants AST96-16964 and AST00-71176 and by the University of Minnesota Supercomputing Institute. The work by D.R. was supported in part by KRF through grant KRF-2000-015-DS0046. We gratefully acknowledge Larry Rudnick for many helpful comments and discussions.

Table 1. Summary of Simulations

Model <sup>a</sup>	ID	In-flowing Electrons <sup>b</sup> ( $b_1$ )	Shock Injection Parameter ( $\epsilon$ )	Cooling Time <sup>c</sup> (Myr)	$B_{x0}$ ( $\mu G$ )
1.....	Control	$10^{-4}$	0.0	$1.63 \times 10^4$	0.39
2.....	Injection	$10^{-8}$	$10^{-4}$	$1.63 \times 10^4$	0.39
3.....	Cooling	$10^{-4}$	0.0	54	5.7

<sup>a</sup>All models used external Mach 80 jets ( $M_j = u_j/c_a = 80$ ), which corresponded to a velocity of 0.05 c, and a density contrast  $\eta = \rho_j/\rho_a = 0.01$ ; thus the internal jet Mach number is 8. Units derive from  $r_j = 1$  (representing 2 kpc in physical units), an ambient density,  $\rho_a = 1$ , and a background sound speed,  $c_a = (\gamma P_a/\rho_a)^{1/2} = 1$  ( $\gamma = 5/3$ ). The initial axial magnetic field was  $B_{x0}$  ( $\beta = P_a/P_b = 100$ ) in the ambient medium. The jet also carried an additional toroidal field component,  $B_\phi = 2 \times B_{x0}(r/r_j)$ . The spectrum of nonthermal particles in the jet was set to a power law with momentum slope  $q = 4.4$ , which corresponds to a synchrotron spectral index  $\alpha = 0.7$ . The nonthermal particle distribution was specified by  $N = 8$  momentum bins in all three models.

<sup>b</sup>Ratio of nonthermal to thermal electron density in the incident jet flow.

<sup>c</sup>Time for electrons to cool below momentum  $\hat{p} = 10^4 m_e c$  in the background magnetic field  $B_{x0}$ . In these simulations the time unit  $r_j/c_a$  corresponds in physical units to approximately 10 Myr.

## REFERENCES

- Begelman, M. C., Blandford, R. D., & Rees, M. J. 1984, *Rev. Mod. Phys.*, 56, 255
- Begelman, M. C. & Cioffi, D. F. 1989, *ApJ*, 345, L21
- Blandford, R. D. & Rees, M. J. 1974, *MNRAS*, 169, 395
- Blundell, K. M. & Rawlings, S. 2000, *AJ*, 119, 1111
- Bridle, A. 1992, in *AIP Conf. Proc. 254, Testing the AGN Paradigm*, ed. S. Holt, S. G. Neff, & C. M. Urry (New York: AIP), 386
- Bykov, A. M. & Uvarov, Y. A. 1999, *JETP*, 88, 465
- Carilli, C. L., Perley, R. A., & Dreher, J. H. 1988, *ApJ*, 334, L73
- Carilli, C. L., Perley, R. A., Dreher, J. H., & Leahy, J. P. 1991, *ApJ*, 383, 554
- Clarke, D. A. 1993, in *Proceedings of the Ringberg Workshop, Jets in Extragalactic Radio Sources*, ed. H.-J. Röser & K. Meisenheimer (Berlin: Springer), 243
- Clarke, D. A. 1996, in *ASP Conf. Ser. 100, Energy Transport in Radio Galaxies and Quasars*, ed. P. E. Hardee, A. H. Bridle, & J. A. Zensus (San Francisco: ASP), 311
- Clarke, D. A., Norman, M. L., & Burns, J. O. 1989, *ApJ*, 342, 700
- Clarke, T. E., Kronberg, P. P., & Böhringer, H. B. 2000, *Cluster Mergers and their Connection to Radio Sources*, 24th meeting of the IAU, Joint Discussion 10, August 2000, Manchester, England., 10, E17
- Condon, J. J. & Mitchell, K. J. 1984, *ApJ*, 276, 472
- Cox, C. I., Gull, S. F., & Scheuer, P. A. G. 1991, *MNRAS*, 252, 558
- Downes, T. P., Duffy, P., & Komissarov, S. 2001, *MNRAS*, in press
- Eilek, J. A., Melrose, D. B., & Walker, M. A. 1997, *ApJ*, 483, 282
- Evans, C. R. & Hawley, J. F. 1988, *ApJ*, 332, 659
- Falle, S. A. E. G. 1991, *MNRAS*, 250, 581
- Frank, A., Ryu, D., Jones, T. W., & Noriega-Crespo, A. 1998, *ApJ*, 494, L79
- Gieseler, U. D. J. & Jones, T. W. 2000, *A&A*, 357, 1133

- Gooch, R. E. 1995, in ASP Conf. Ser. 101, *Astronomical Data Analysis Software and Systems V*, ed. G. H. Jacoby & J. Barnes (San Francisco: ASP), 80
- Hardee, P. E., Clarke, D. A., & Rosen, A. 1997, *ApJ*, 485, 533
- Hardee, P. E. & Norman, M. L. 1990, *ApJ*, 365, 134
- Hardee, P. E. & Rosen, A. 1999, *ApJ*, 524, 650
- Harten, A. 1983, *J. Comp. Phys.*, 49, 357
- Hines, D. C., Owen, F. N., & Eilek, J. A. 1989, *ApJ*, 347, 713
- Hughes, P., Duncan, C., & Mioduszewski, A. 1996, in ASP Conf. Ser. 100, *Energy Transport in Radio Galaxies and Quasars*, ed. P. E. Hardee, A. H. Bridle, & J. A. Zensus (San Francisco: ASP), 137
- Icke, V. 1991, in *Beams and Jets in Astrophysics*, ed. P. A. Hughes (New York, New York: Cambridge Astrophysics Series), 232
- Jones, T. W., O'Dell, S. L., & Stein, W. A. 1974, *ApJ*, 188, 353
- Jones, T. W., Ryu, D., & Engel, A. 1999, *ApJ*, 512, 105, (JRE99)
- Kaiser, C. R. 2000, *A&A*, 362, 447
- Katz-Stone, D. M. & Rudnick, L. 1997, *ApJ*, 488, 146
- Kellermann, K. I. & Owen, F. N. 1988, in *Galactic and Extragalactic Radio Astronomy*, ed. G. L. Verschuur & K. I. Kellermann (New York: Springer-Verlag), 563–602
- Kössl, D., Müller, E., & Hillebrant, W. 1990, *A&A*, 229, 378
- Laing, R. A. 1981, *ApJ*, 248, 87
- Lind, K., Payne, D., Meier, D., & Blandford, R. 1989, *ApJ*, 344, 89
- Lonsdale, C. J. & Barthel, P. D. 1986, *AJ*, 92, 12
- Looney, L. W. & Hardcastle, M. J. 2000, *ApJ*, 534, 172
- Mantovani, F., Junor, W., Valerio, C., & McHardy, I. 1999, *A&A*, 346, 397
- Matthews, A. P. & Scheuer, P. A. G. 1990a, *MNRAS*, 242, 616
- . 1990b, *MNRAS*, 242, 623

- Micono, M., Zurlo, N., Massaglia, S., Ferrari, A., & Melrose, D. B. 1999, *A&A*, 349, 323
- Nishikawa, K., Koide, S., Sakai, J., Christidou, D., Sol, H., & Mutel, R. 1998, *ApJ*, 498, 166
- Norman, M. L. 1996, in *ASP Conf. Ser. 100, Energy Transport in Radio Galaxies and Quasars*, ed. P. E. Hardee, A. H. Bridle, & J. A. Zensus (San Francisco: ASP), 319
- Norman, M. L., Smarr, L., Winkler, K.-H. A., & Smith, M. D. 1982, *A&A*, 113, 285
- Ryu, D. & Jones, T. W. 1995, *ApJ*, 442, 228
- Ryu, D., Jones, T. W., & Frank, A. 1995, *ApJ*, 452, 785
- . 2001, *ApJ*, in press
- Ryu, D., Miniati, F., Jones, T. W., & Frank, A. 1998, *ApJ*, 509, 244
- Sato, T. & The Complexity Simulation Group. 1996, *Phys. Plasmas*, 5, 2135
- Scheuer, P. 1989, in *Hotspots in Extragalactic Radio Sources*, ed. K. Meisenheimer & H.-J. Roser (New York: Springer-Verlag), 159
- Scheuer, P. A. G. 1974, *MNRAS*, 166, 513
- . 1982, in *IAU Symposium 97, Extragalactic Radio Sources*, ed. D. Heeschen & C. Wade (Dordrecht: Reidel), 163
- Skilling, J. 1975, *MNRAS*, 172, 557
- Smith, M. D., Norman, M. L., Winkler, K.-H. A., & Smarr, L. 1985, *MNRAS*, 214, 67
- Spruit, H. C. 2000, in *IAU Symposium 195, Highly Energetic Physical Processes and Mechanisms for Emission From Astrophysical Plasmas*, ed. P. C. H. Martens & S. Tsuruta (San Francisco: ASP), 113
- Sudou, H. & Taniguchi, Y. 2000, *AJ*, 120, 697
- Tregillis, I. L., Jones, T. W., & Ryu, D. 2001a, in *ASP Conf. Series, Particles and Fields in Radio Galaxies*, ed. R. A. Laing & K. M. Blundell (San Francisco: ASP)
- Tregillis, I. L., Jones, T. W., Ryu, D., & Park, C. 2001b, in *Proceedings of the Life Cycles of Radio Galaxies Workshop*, ed. J. Biretta (New York: Elsevier)
- Treichel, K., Rudnick, L., Hardcastle, M. J., & Leahy, J. P. 2001, *ApJ*, in press

Valtaoja, E. 1984, *A&A*, 140, 148

van den Heuvel, E. P. J., Ostriker, J. P., & Petterson, J. A. 1980, *A&A*, 81, L7

Weiss, N. O. 1966, *Proc. R. Soc. London A*, 293, 310

Williams, S. A. & Gull, S. F. 1985, *Nature*, 313, 34

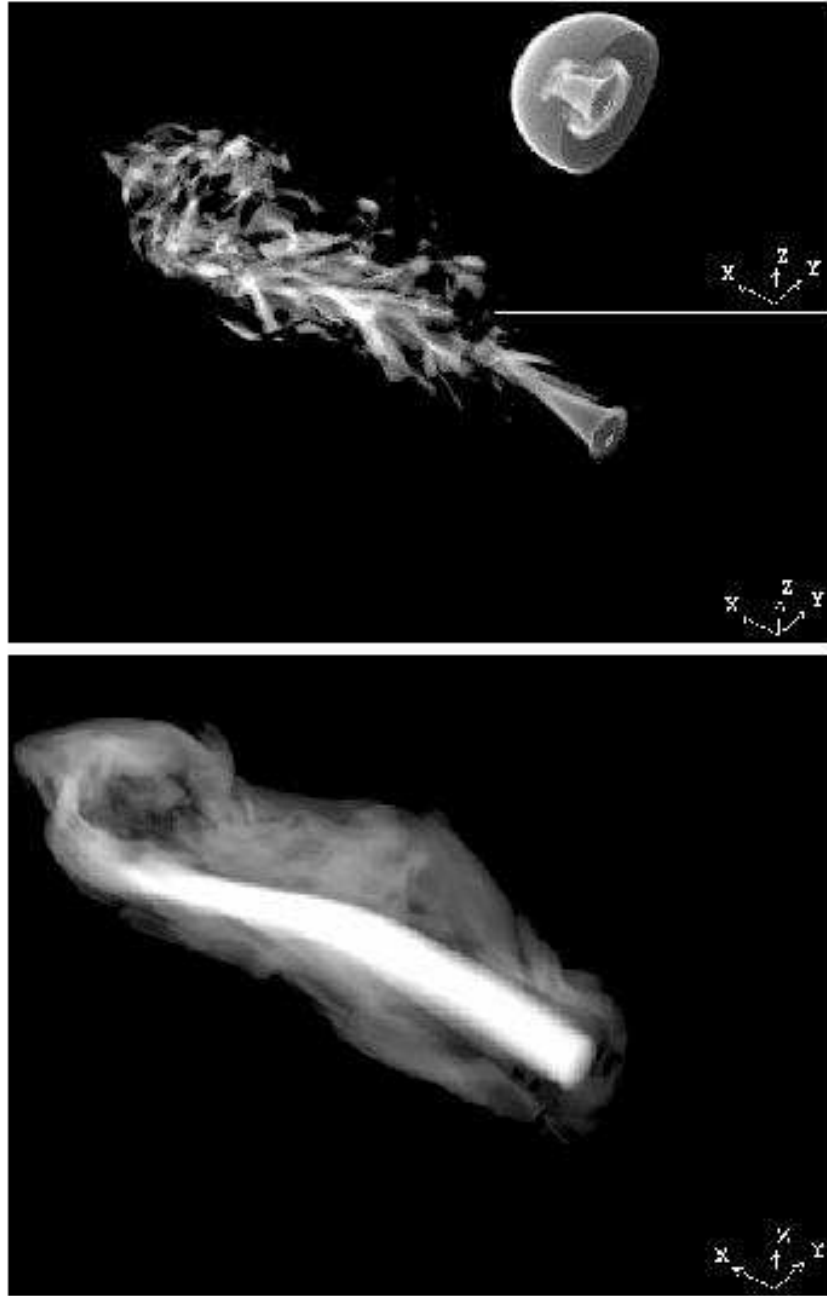


Fig. 1.— (a) Top: Volume-rendered images of the shock structure ( $\nabla \cdot \mathbf{u}$ ) in the jet flow. The inset shows the situation at  $t = 0.7$ , prior to breakup of the terminal Mach disk, where the background has not been filtered out in order to make the bow shock visible. The main image shows the “shock-web complex” at  $t = 4.0$ , for zones containing only jet-supplied material ( $C_j \geq 0.99$ ). The small square in the lower right marks the jet orifice, and the orientation corresponds to the jet pointing slightly out of the page. (b) Bottom: Volume-rendered jet velocity magnitude ( $|\mathbf{u}|$ ) at  $t = 4.0$ . The orientation is the same as in (a), and ambient material has been filtered out ( $C_j \geq 0.99$ ).



Fig. 2.— (a) Top: Volume-rendered image of log of thermal plasma pressure at  $t = 4.0$ . Displayed pressures span a range of  $10^2$ . (b) Bottom: Volume-rendered image of log of magnetic pressure at  $t = 4.0$ . Displayed pressures span range of  $10^3$ . Most of the largest values are found in the jet core. Large volumes of the cocoon are occupied by magnetic pressures more than two orders of magnitude below the nominal value in the jet. In both images, only material with  $C_j \geq 0.99$  is shown.



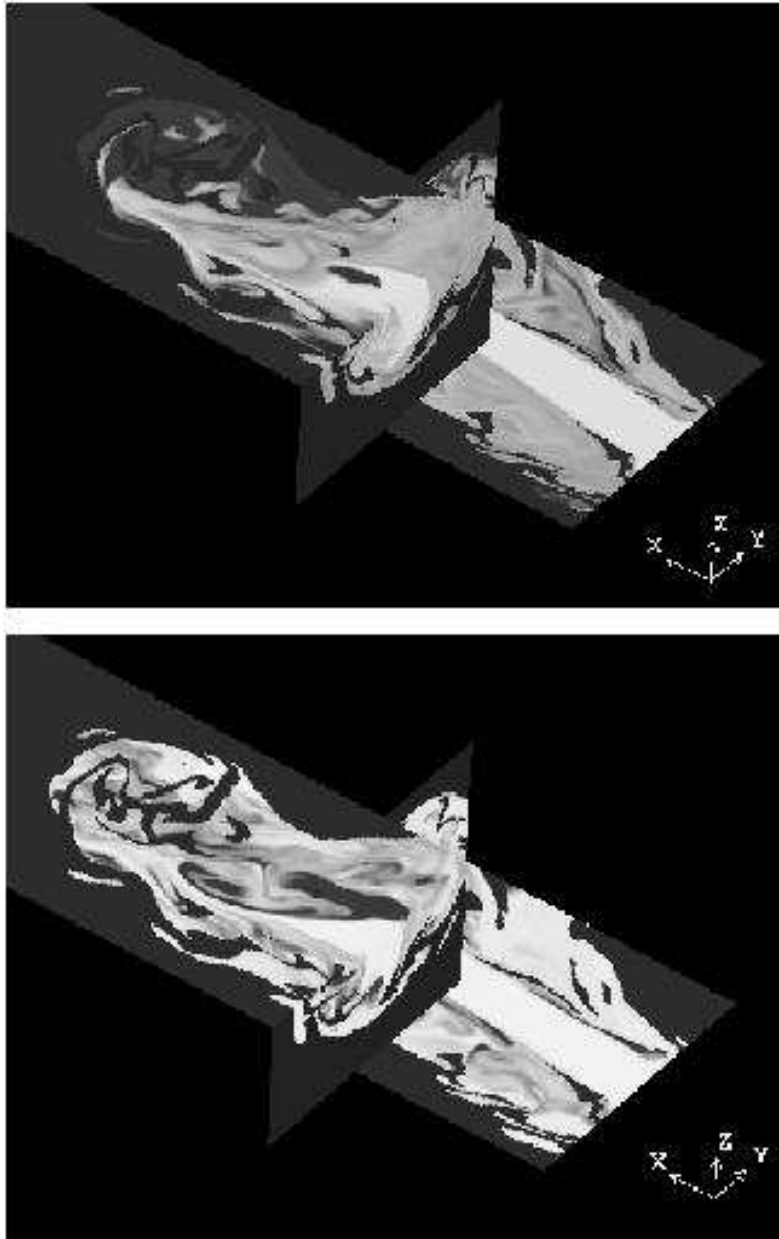


Fig. 3.— (a) Top: Orthogonal slices through the computational grid, showing nonthermal electron momentum indices  $q$  for electrons with  $p \approx 3 \times 10^4$  in model 2 at  $t = 4.0$ . Notice the variegated spectral structure of the cocoon. As usual, electrons entering with the jet have  $q = 4.4$ , but now fresh-particle injection at the myriad weak shocks in the shock web leads to an excess of steep-spectrum electrons in the head region. The display range is  $4 < q < 7$ , with the flattest material light. (b) Bottom: Corresponding image for model 3. The spectral structure of the cocoon is quite patchy, lacking both the uniformity of model 1 and the overall gradient of model 2. Here the display range is larger, with  $4 < q < 9$  to capture the effects of radiative aging. In both images only material with  $C_j \geq 0.99$  is shown.

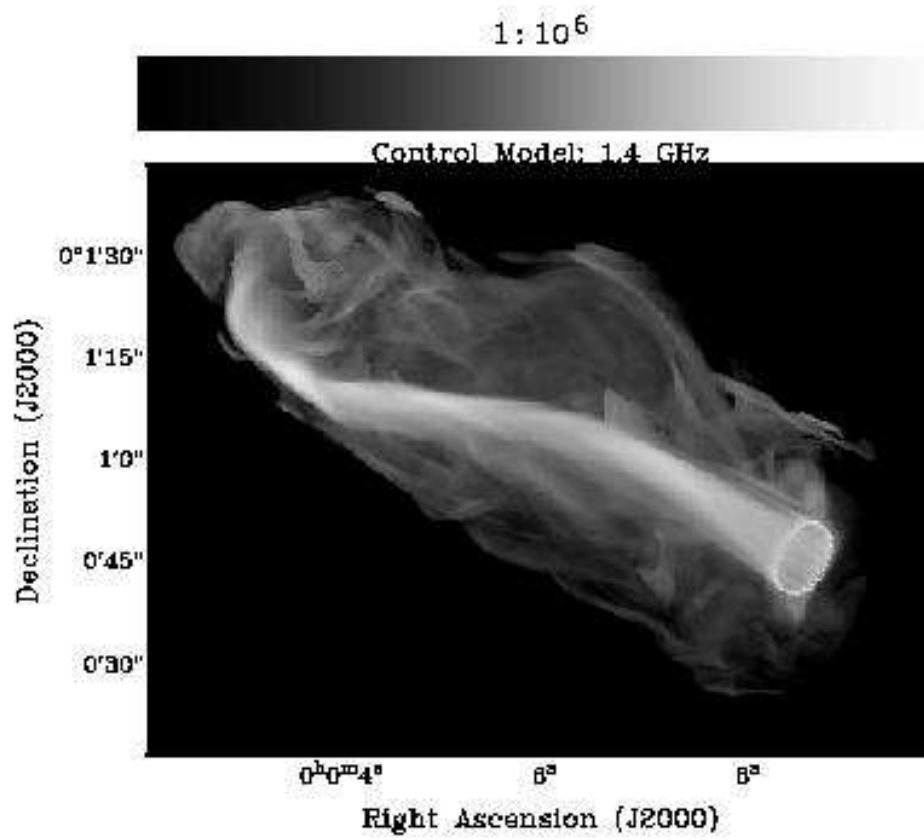


Fig. 4.— Model 1 synchrotron surface brightness map calculated at  $\nu = 1.4$  GHz, time  $t = 4.0$ . The source orientation in this image corresponds to that in the preceding images.

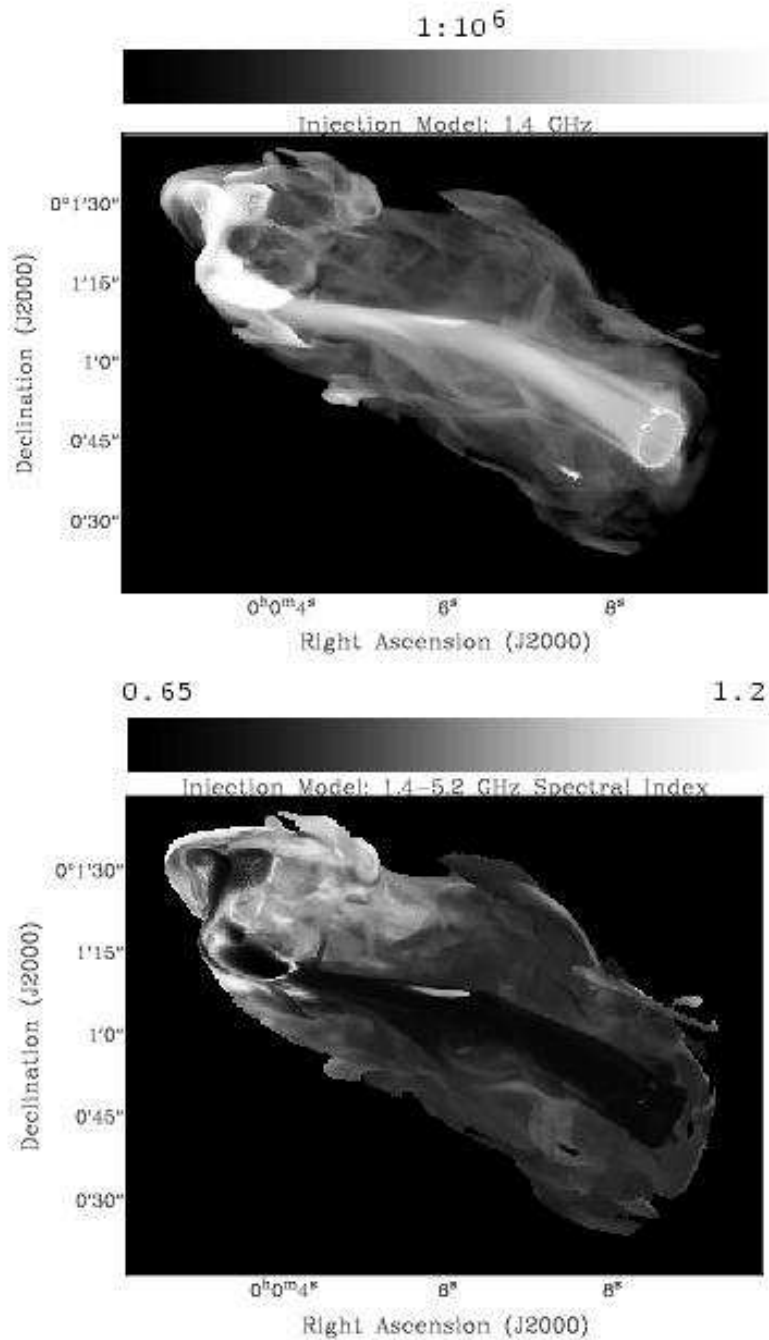


Fig. 5.— (a) Top: Model 2 synchrotron surface brightness map calculated at  $\nu = 1.4$  GHz, time  $t = 4.0$ . (b) Bottom: Model 2 synchrotron spectral index map calculated from surface brightness maps at  $\nu = 5.2$  GHz and  $\nu = 1.4$  GHz, time  $t = 4.0$ .

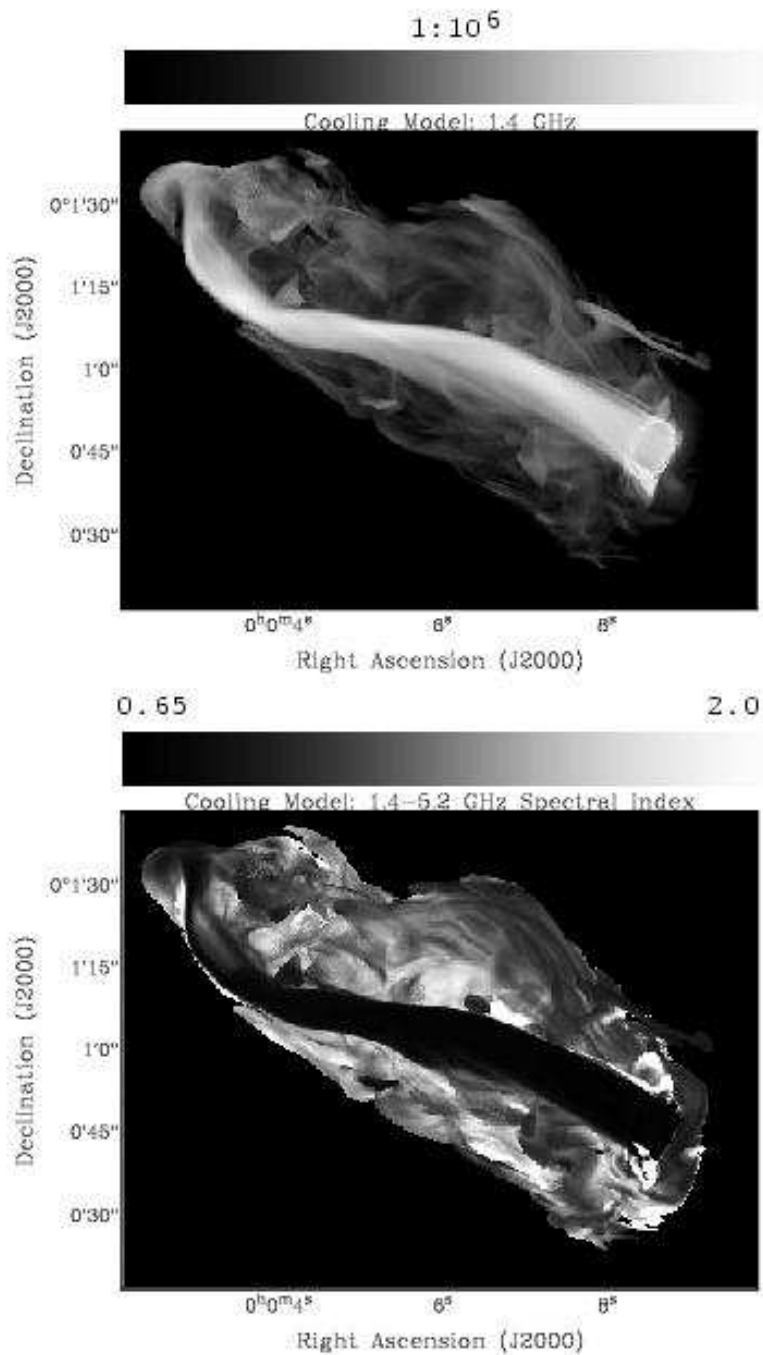


Fig. 6.— (a) Top: Model 3 synchrotron surface brightness map calculated at  $\nu = 1.4$  GHz, time  $t = 4.0$ . (b) Bottom: Model 3 synchrotron spectral index map calculated from surface brightness maps at  $\nu = 5.2$  GHz and  $\nu = 1.4$  GHz, time  $t = 4.0$ .